Review Article

INORGANIC CHEMISTRY RESEARCH
Published by the
Iranian Chemical Society
www.inorgchemres.org
info@inorgchemres.org

***Inorg. Chem. Res.**, Vol. 4, No. 2, 140-182, December 2020*
DOI: 10.22036/icr.2020.233174.1062

Inorganic Nanostructures Especially Obtained from Liquid/Liquid Interface by Reduction of Organometallic Precursors: A Mini Review

S. Jafar Hoseini*,†, Mehrangiz Bahrami and S. Masoud Nabavizadeh

Professor Rashidi Laboratory of Organometallic Chemistry, Department of Chemistry, College of Sciences, Shiraz University, Shiraz, 7194684795, Iran

†*Dedicated to the Memory of Prof. Mehdi Rashidi for his Outstanding Contributions to Organometallic Chemistry*

(Received 29 May 2020, Accepted 17 August 2020)

The synthesis routes for the preparation of nanostructures have been developed in the past decade. Organometallic precursors played an important role in the synthesis of nanomaterials *via* various methods of synthesis. In this investigation, nanostructures were synthesized from organometallic precursors and applied as catalyst in various reactions. This mini review is mostly devoted to the research efforts carried out by our group on the search for new classes of organometallic precursors and applying them for the synthesis of nanostructured catalysts with different morphologies. Also we have investigated the effect of alloying and presence of support on catalytic activity. We found that stabilization of nanostructures on graphene oxide, aminoclay, ionic liquids or cyclodextrin supports can increase the catalytic activity by increasing the stability and dispersion. Furthermore, alloyed nanostructures can be efficient like noble metal catalysts in catalytic applications. Also, thin films fabricated by this method showed higher quality in comparison with the thin films fabricated by other synthetic methods.

Keywords: Toluene-water interface, Nanoparticle, Suzuki-Miyaura reaction, Fuel cell

INTRODUCTION

Synthesis of nanomaterials has been developed over the last two decades; but this development was restricted to just few groups of nanomaterials such as quantum dots, iron oxides and plasmonic nanoparticles (NPs) with a controlled size and morphology which reined by standard and physical chemistry approaches [1]. Great interests have been attracted by inorganic nanostructures (nanowires, nanotubes, *etc.*) due to their important role in technological applications for new devices [2-4]. From few years ago, organometallic precursors were applied for the synthesis of large variety of nanomaterials with a clean and controllable surface. These kinds of nanomaterials exhibit interesting physical, chemical and catalytic properties. This mini-review describes the research efforts carried out nearly by our group on applying and developing the new groups of precursors for the synthesis of inorganic nanomaterials with different morphologies obtained from different strategies such as liquid-liquid interface and investigating their important applications in hydrogenation, C-C coupling and methanol oxidation of direct methanol fuel cell (DMFC) reactions [5-29].

NPs are a class of important materials with different types in science and technology. The first scientific synthesis of NPs is attributed to Faraday's investigation on gold colloids [30] and developed by the availability of diverse microscopic characterization techniques. Classification of NPs is based on their morphology, dimensionality and composition. The metallic nanostructures are applied extensively in the fields of catalysis, electronics, medicine, etc. Apart from these, their efficacy as antibacterial agents [31] and superconductors [32] has also been investigated. Chemical strategies have emerged to be indispensable for the synthesis of various types of nanomaterials which are generally carried out

*Corresponding author. E-mail: sj.hoseini@shirazu.ac.ir

under mild conditions. Reduction method is one of the best strategies in the presence of alcohols, borohydride, citrate, *etc.* [33]. To reduce the soluble metal precursors and obtain the corresponding metals with zero oxidation state, various reducing agents were used. By terminating the growth with appropriate surfactants or ions, metal NPs are produced. One of the reduction methods is the borohydride reduction, known since the 1950s and was one of the subjects of investigation under the Manhattan project [34]. A direct hydride transfer mechanism [35] is proposed for the reduction of [$PtCl_2$(cod)] (cod: *cis,cis*-1,5-cyclooctadiene) by $NaBH_4$. $NaBH_4$ is hydrolyzed in water to BO_2^- ion and H_2 gas. BO_2^- can change to boric acid with a low toxicity (Eqs. (1) and (2)).

$$BH_4^- + 2H_2O \longrightarrow BO_2^- + 4H_2 \quad (1)$$

$$BO_2^- + 2H_2O \longrightarrow H_3BO_3 + OH^- \quad (2)$$

Liquid-liquid interface strategy reached the attention of scientists in synthetic chemistry nearly 130 years after Schotten and Baumann. In modern chemistry, reactions "on water", "at the interface" or by "phase-transfer" are important platforms for synthesis [36]. These kinds of reactions are applicable in electrochemistry, NPs synthesis, heterogeneous catalysis and solvent extraction fields [37-40]. The interface between two immiscible liquids like toluene-water produce unique environment for the synthesis of nanomaterials with remarkably different structural, dynamical and thermodynamic properties in comparison with the nanomaterials prepared by other procedures. The progress in this field has been developed by Rao *et al.* [41-45] and continued and completed by Hoseini and co-workers [5-29]. Figures 1a-c shows the formation of metallic thin film at toluene-water interface. A reduction in the interfacial energy between the two phases of toluene and water is the reason of the particles assembly at the interface [5], which is expressed as the difference between the energies of the oil-water ($\gamma_{O/W}$), the particle-water ($\gamma_{P/W}$) and the particle-oil ($\gamma_{P/O}$) interfaces. The relation between the three interfacial energies and contact angle, θ, is described by Young's equation as follow (Eq. (3)):

$$\cos\theta = (\gamma_{PO} - \gamma_{PW})/\gamma_{OW} \quad (3)$$

For the contact angle of 90° (Fig. 1c), thin film formation is occurred at the interface [5]. Tendency to the decrease of energy is the reason why particles are assembled at the interface (Fig. 1c). In other words, the fact that favours the attachment and assembly of particles dispersed in liquid phases is the high energy interface between the two liquids, which leads to the overall system energy reduction [5]. Nature of the interface, surface modification and radius of the NPs are important facts in the assembly process at the liquid-liquid interface [46]. It can be concluded that liquid-liquid interfaces provide defect-free support for NPs formation and self-assembly. Remaining all particles at the interface depends on the rate of reducing agent addition and the size of drops. Addition of very small drops of reductant with a very low rate and minimal disturbing the interface remains all the particles at the interface and produce a thin film [5-29].

Volkov *et al.* have investigated the applications of liquid-liquid interfaces in the chemical, biological and pharmaceutical fields [47]. This strategy is also fundamental in many industrial applications such as solvent extraction, drug delivery and electrochemical energy storage devices. It is obvious that the interface between two immiscible liquids offers an important platform for the synthesis of various nanostructures with novel applications [48-50].

SYNTHESIS OF NANOMATERIALS

Nanomaterials are synthesized by applying different chemical and electrochemical methods. In liquid-liquid interfaces synthesis, the properties of interfaces depend on the nature of the species, their concentrations, the polarity of immiscible solvents and temperature. Among different applied methods, reduction of the metallic precursor is better due to our good experience [5-29].

Nanomaterials at Liquid-Liquid Interfaces, Synthesis of Nanomaterials from Organometallic Precursors

We have used the organometallic precursors for the synthesis of different nanostructures at liquid-liquid interface. This facile method is developed for the synthesis

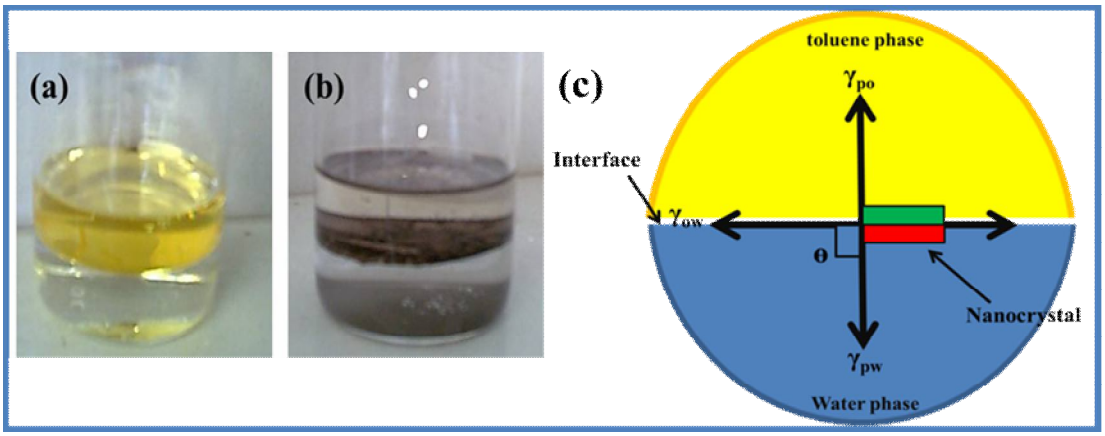

Fig. 1. (a) Organometallic complexes dissolved in toluene (top phase) and water (bottom phase), (b) Formation of metallic thin film at toluene-water interface, (c) Schematic illustration of the thin film formation at liquid-liquid interface.

of monometallic nanostructures, bi, tri and tetrametallic alloys and metal-organic frameworks [5-29].

Organometallic complexes with one or more metal atoms and carbon containing species or hydrides play a key role in the synthesis of nanomaterials. The bond between metal and carbon can be a (σ) or (π), such as metal-alkyl and metal-dienes. In these complexes, such as $Cp^*Ir(Me)_4$, with the formal oxidation state between (0)-(V), for Pt and right side elements of the periodic table, the real oxidation state is lower than the formal one due to the covalent nature of the metal carbon bond. These properties have prompted researchers to apply these compounds as precursors to synthesize the newer nanomaterials in spite of their high cost and sometimes hard preparation [51]. Some advantages that encourage chemists to use these compounds to synthesize nanomaterials are: (i) decomposition in a mild condition helps us to have more control on the formation of nanomaterials; also nanomaterials can grow in a milder condition; (ii) clean synthesis of nanomaterials with no salts or impurity on the surface of the as-prepared nanostructures. In the field of metals Schmid prepared Au_{55} clusters by reducing $AuClPPh_3$ (PPh_3: triphenylphosphine) with B_2H_6 [52]. Also, Chaudret *et al*. used organometallic precursors for the formation of nanomaterials [53]. Applying organometallic complexes as precursor for the synthesis of various kinds of nanomaterials with interesting catalytic activity is developed by us [5-29]. In this mini-review, we will discuss briefly the formation of different nanostructures and shed light their excellent catalytic activity.

Toluene-water interface assembly was used for the preparation of monometallic nanomaterials, multimetallic nanoalloys and metal-organic frameworks. In this assembly, organometallic precursors such as $[PtCl_2(cod)]$ [54], $[PdCl_2(cod)]$ [55] and also some other precursors such as $[Ni(acac)_2]$, $[Zn(acac)_2]$, $[Fe(acac)_3]$ [56], *etc.* (acac stands for acetylacetonate) are dissolved in toluene by using ultrasonic waves and contacted with water (as a second phase). Very good solubility in the organic solvents such as toluene and also easy loss of (cod) ligand are the main reasons for choosing (cod) complexes as precursors. The reaction is initiated by dropwise addition of aqueous solution of $NaBH_4$ that leads to the formation of metallic thin films after 24 h [5-29] (Eq. (4)).

$$PtCl_2(cod) + 2\ NaBH_4 + 6\ H_2O \longrightarrow Pt(0) + 2\ NaCl + 2\ H_3BO_3 + 7\ H_2 + cod \quad (4)$$

Pt(0) and Pd(0) monometallic thin films were synthesized at liquid-liquid interface by applying different organometallic/non-organometallic complexes. Thin films formation was completed after 24 h (Scheme 1a). To remove the product from the interface, the toluene phase

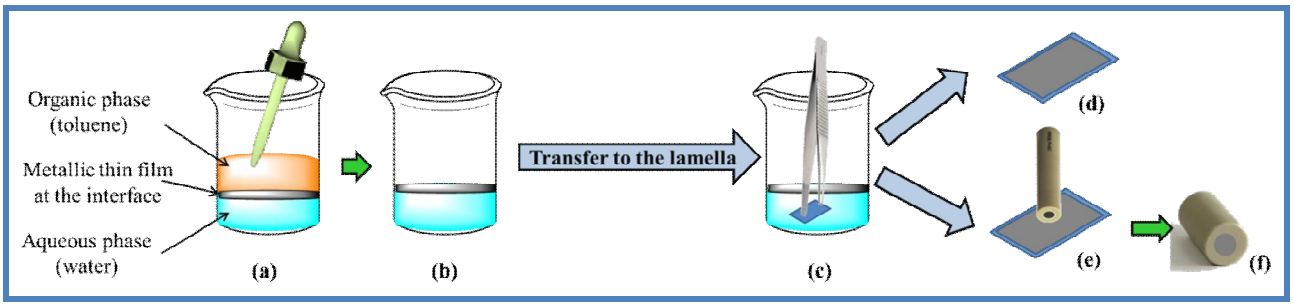

Scheme 1. (a) Thin film formation at toluene-water interface, (b) removing the toluene phase, (c) transferring the thin film to the glassy lamella, (d) thin film was air-dried on a lamella, (e) transferring the wet film to the glassy carbon surface, (f) glassy carbon electrode after air-drying

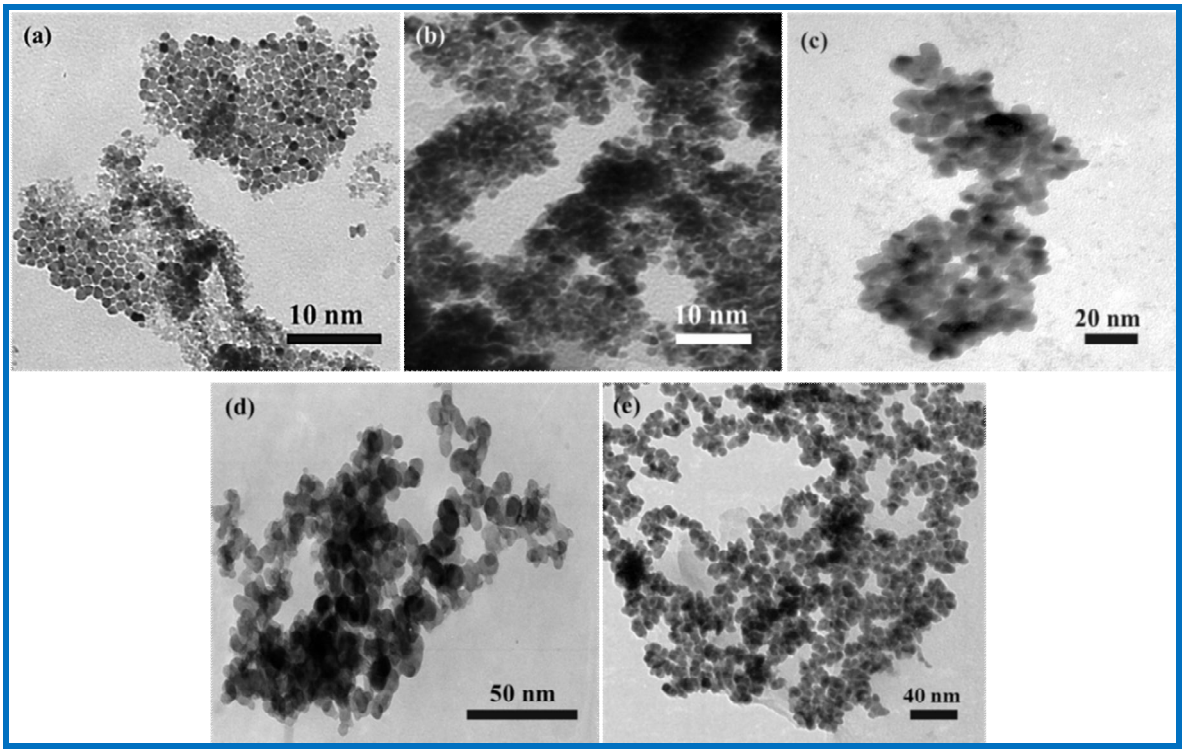

Fig. 2. TEM images of Pt(0)/ Pd(0) thin films obtained from (a) [$PtCl_2$(cod)] [6], (b) [PtI_2(cod)] [6], (c) [Pt(*p*-tolyl)$_2$(SMe_2)$_2$] [6], (d) [$PtCl_2$(SMe_2)$_2$] [5] and (e) [$PdCl_2$(cod)] [7] complexes.

should be removed from the top phase using a dropper (Scheme 1a and b). For separation of thin film, a glassy lamella and forceps were used. The lamella was immersed under the thin film, brought up (Scheme 1c) and thin film was air-dried on a lamella (Scheme 1d), but for transferring the thin film to the surface of electrode, wet film was used following by squeezing the glassy carbon surface on the thin layer up to became dry (Scheme 1e) and then air-dried

(Scheme 1f).

As it is obvious in transmission electron microscopy (TEM) images, the as-synthesized NPs exhibit different morphologies and sizes (Figs. 2a-e) that affect the catalytic activity. Monodispersed well organized spherical Pt(0) NPs with the mean diameter of 2 nm were obtained using $[PtCl_2(cod)]$ precursor (Fig, 2a) [6]. Applying $[PtI_2(cod)]$ as a precursor was led to the formation of agglomerated spherical NPs with 4.6 nm diameter (Fig, 2b) [6]. By comparing these results, it can be concluded that halogen ions played an important role on growing process of the Pt(0) NPs. This fact is similar to the use of KBr to achieve shape control of Pd NPs [57] or different reports on effective influence of anions on the morphology of NPs [58, 59]. Figure 2c exhibits the agglomerated spherical NPs for Pt(0) thin film with 4-6 nm mean diameter obtained from $[Pt(p\text{-tolyl})_2(SMe_2)_2]$ precursor [6]. Reduction of $[PtCl_2(SMe_2)_2]$ precursor resulted in the formation of a thin film containing connected chains of Pt NPs with 5-6 nm mean diameter (Fig. 2d) [5]. Spherical Pd(0) NPs with high dispersity was formed by the reduction of $[PdCl_2(cod)]$ (Fig. 2e). The mean diameter was approximately 4 nm [7].

Bi, Tri and Tetrametallic Nanoalloy Thin Films Formation Using Alloying Strategy

Multi-metallic NPs have extracted intensive attention due to their important role in catalysis and Pt and Pd-based NPs are considered more attention due to their higher activity in various catalytic reactions [60-62]. Catalysts with distinct properties from their monometallic counterparts can be obtained by mixing two or more metals. Compare with single phase of metal nanostructures, mixed metal nanostructures can provide a more effective way in the exploration of catalysts with enhanced performance due to their multiple reaction sites. Therefore, replacing the high cost Pt metal is in progress and only alloys of some few transition metals have shown activity close to or comparable to that of Pt. Pd is one of these transition metals with lower cost than Pt and is highly electroactive for small organic molecule oxidation. Meanwhile, the electrocatalytic activity of Pd can obviously be improved by the addition of a third or fourth element, such as transition metal Ni, Zn or Fe due to the trimetallic and tetrametallic promotional effect. The main factors that affect the catalytic activity are electronic and geometric effects, mainly influencing the catalytic performance of noble metal materials. Therefore, besides the components, the size and surface morphology of electrocatalysts are also crucial for their catalytic activities. Nanostructures with different morphologies exhibit different atomic arrangements on the surface resulting in distinct electronic and geometric structures and improving the catalytic activity [8]. Noble metal alloy nanostructures with nanobranch (NB) morphologies such as nanodendrimers are promising candidates for electrocatalytic reactions due to their large surface area and high active sites. Furthermore, nanosheets are an important class of materials that are highly attractive due to their high surface area to volume ratio [63]. This characteristic makes the nanosheets highly useful for catalysis, chemical sensing, and surface enhanced Raman scattering applications [64]. Based on these factors, formation of noble metal alloy nanostructures is necessary and leads to catalytic activity improvement. Figure 3 shows the TEM images of bimetallic alloys obtained at toluene-water interface. PtPd snowman-like structures (Fig. 3a) [25a], $PtFeFe_2O_3$ [12] and PdZn spherical NPs (Fig. 3b,c) [19], PtCo nanosheets (Fig. 3d) [25b], PtSn nanotubes (Fig. 3e) [10], PdCu [17], PdNi [8] and PtNi [8] spherical NPs (Figs. 3f,g,h) are observable. Also, PtPdNi [8] and PtPdNiZn [8] alloy nanosheets (ANSs) as new catalysts are expected to attract much interest because of the special conjunct effects of alloys and nanosheets. However, up to now, it still remains a great challenge to find a method to fabricate the well-defined tri and tetrametallic ANSs.

Based on the above considerations, we have synthesized spherical PtPdCu [17] and PtPdZn [19] trimetallic alloy thin films (Figs. 4e and f) at toluene/water interface by the reduction of the suitable complexes at the interface. Also, PdNiZn (Fig. 4a,b) [15], PtPdNi (Figure 4c) [8] and PtZnSn (Fig. 4d) [11] ternary ANS with low Pt content *via* liquid-liquid interface strategy was synthesized, having the following advantages: (i) the second and third metal elements, such as Pd and Ni, can be easily reduced simultaneously with Pt to form PtPdNi ternary alloy, (ii) the PtPdNi ANSs are easily synthesized and most of the catalytically active atoms are on the surface, maximizing the efficiency in their use, which is predominantly favorable for the amount of the precious metals. Furthermore, tetrametallic alloys such as $PtPdNiFeFe_2O_3$ nanodendrimers

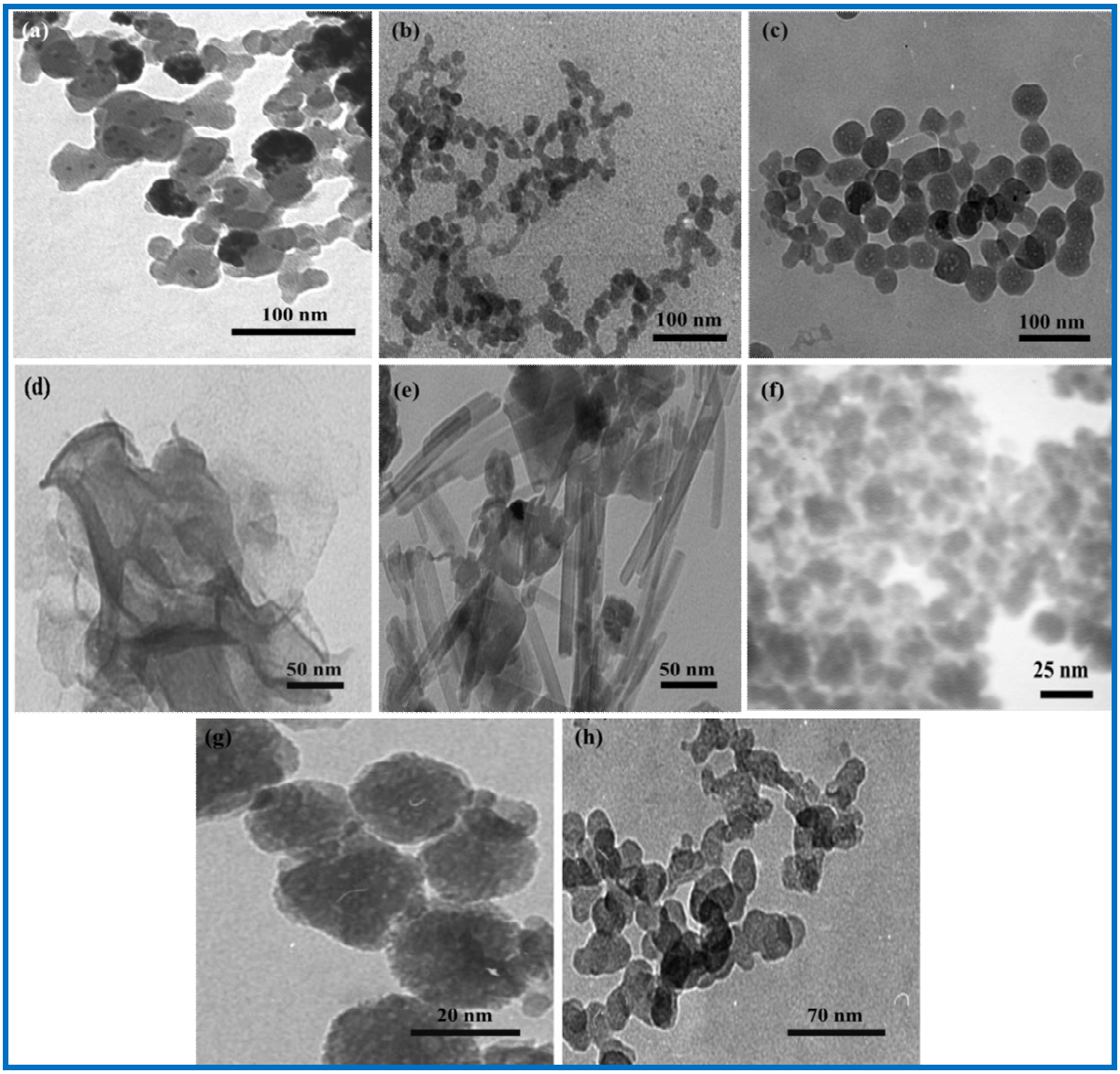

Fig. 3. TEM images of bimetallic nanoalloys of (a) PtPd [25a], (b) $PtFeFe_2O_3$ [12], (c) PdZn [19], (d) PtCo [25b], (e) PtSn [10], (f) PdCu [17], (g) PdNi [8] and (h) PtNi [8] thin films.

(Figs. 5a,b) [8], PtPdNiSn NPs (Fig. 5c) [8] and PtPdNiZn nanosheets (Fig. 5d) [8] were synthesized at toluene-water interface. In this research, we have been able to improve the catalytic activity and minimize the usage of precious metals that lead to a lower cost. The results reported in this investigation prove that the fabricated PtPdNi and PtPdNiZn ANSs, and $PtPdNiFeFe_2O_3$ nanodendrimers exhibit remarkable electrocatalytic activity for methanol oxidation.

One of the routes for the synthesis of nanodendrites is seed-mediated diffusion coupled with the aggregation route with a core of one metal attached by the branched arms of another metal [65]. The reduction rate is the most important factor for controlling the rate of nucleation and growth. Drop-wise addition of $NaBH_4$ to the stabilized mixture of

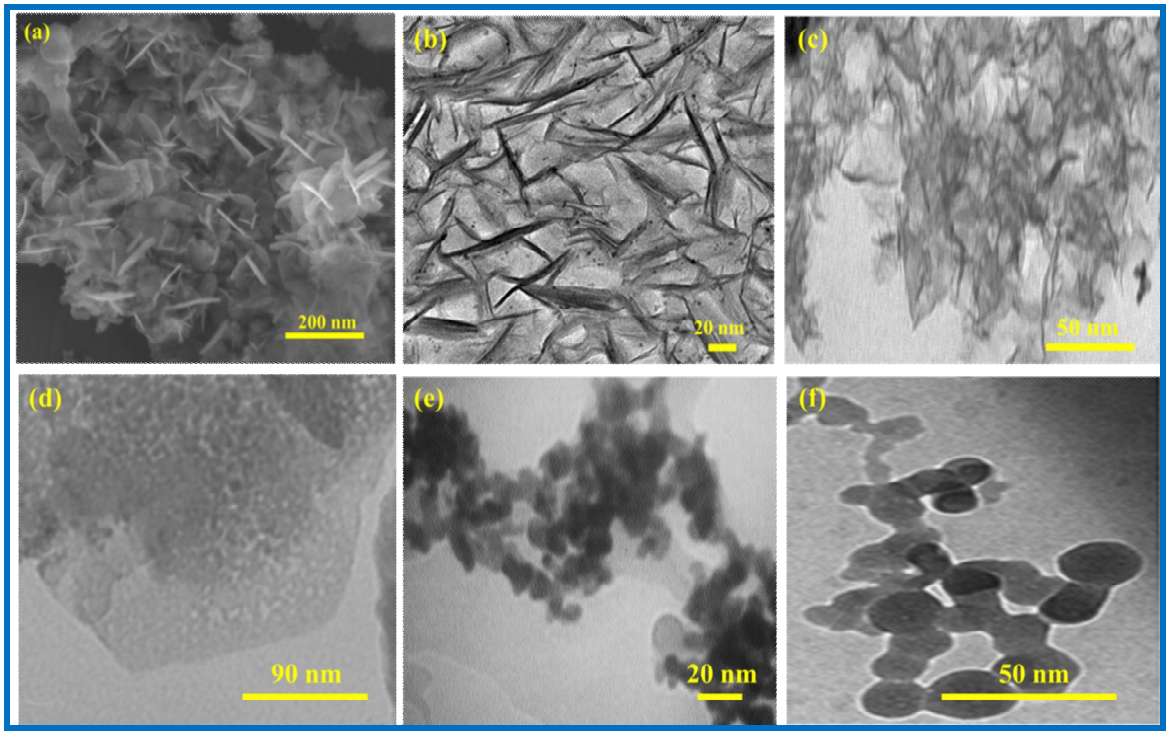

Fig. 4. (a) Scanning electron microscopy (SEM) image of PdNiZn [15], TEM images of (b) PdNiZn [15], (c) PtPdNi [8], (d) PtZnSn [11], (e) PtPdCu [17] and (f) PtPdZn [19].

$[PtCl_2(cod)]$, $[PdCl_2(cod)]$, $[Ni(acac)_2]$ and $[Fe(acac)_3]$ in toluene (top phase) and water leads to metal precursors reduction. The reduction process occurs according to the values of standard electrode potentials for each metal. Reduction of the platinum(II) precursor is the first reaction that leads to Pt(0) NPs (Scheme 2a). In situ formed seeds of Pt(0) act as nucleation sites for further growth. The second metal precursor is a Pd(II) precursor that leads to Pd(0) by the reduction process occurring and snowman-like PtPd bimetallic alloys synthesized on Pt NP seeds at the liquid-liquid interface (Scheme 2b). The aggregation occurs by keeping on with the addition of $NaBH_4$ with more reduction of platinum and palladium precursors to Pt(0) and Pd(0) (Scheme 2c). In this growth mode, smaller particles with a high surface energy are produced in the nucleation stage through the reduction of metal precursors, and aggregate to each other to minimize the total surface energy. By keeping on with the addition of $NaBH_4$ reducing agent, dendritic structures are prepared (Scheme 2d and e). By the reduction of, respectively, iron and nickel precursors, pre-synthesized branched PtPd seeds were used to generate the alloy $PtPdNiFeFe_2O_3$ NBs by diffusion of Fe and Ni into the seeds (Scheme 2f) and the tetrametallic nanodendrite structures are well formed (Scheme 2g).

Metallic NPs Immobilized on Stabilizer

Nanomaterials formed at liquid-liquid interface may be aggregate into a bulk structure due to their high surface energies following by decrease in their catalytic activities [66]. Also, the stability of nanostructures is important. Therefore, immobilization of noble metal NPs on some solid supports such as graphene oxide (GO), aminoclay (AC), ionic liquids (ILs) and β-cyclodextrin with remarkable properties can solve some shortages of these catalysts. The stabilized NPs are good candidates for various catalytic, optical, magnetic, mechanical and electrical applications. Graphene with its two-dimensional

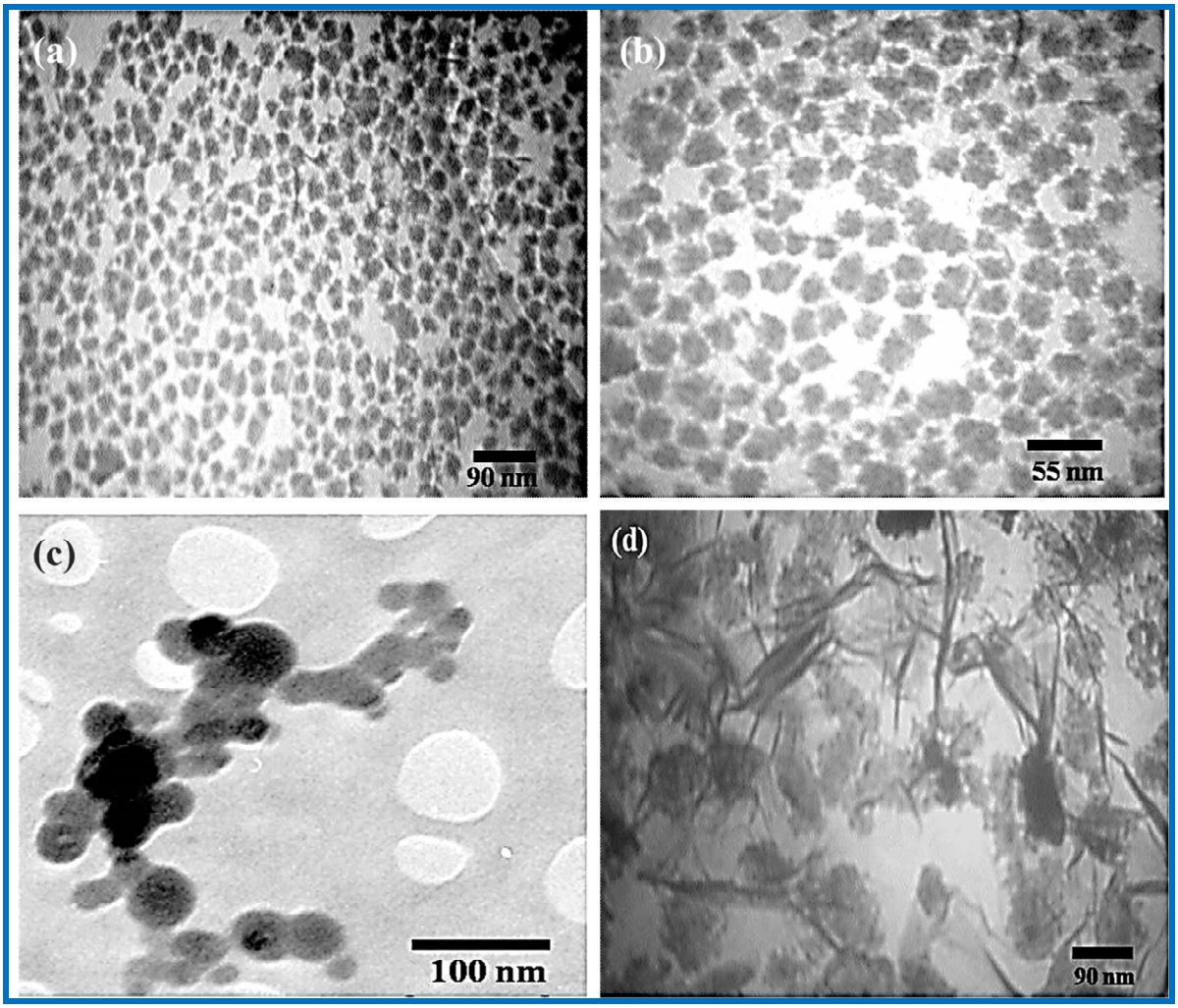

Fig. 5. TEM images of (a,b) $PtPdNiFeFe_2O_3$ nanodendrites [8], (c) PtPdNiSn NPs [8] and (d) PtPdNiZn nanosheets [8] obtain from toluene-water interface.

configuration can be used as a significant catalyst support and also can provide significant electrical conductivity and high surface area [9]. Cooperation of metal NPs and graphene increases the availability of these nanostructures surface area for electron transfer. Also, AC with a magnesium phyllosilicate structure and aminopropyl pendant groups linked to the silicon by covalent attachment, is used as catalyst support. Furthermore, a new support (RGO-AC) is produced *via* a ring-opening reaction between the amine groups of AC and the epoxy group of GO (Scheme 3) [18]. RGO stands for reduced-graphene oxide.

This new stabilizer is characterized by field emission-scanning electron microscopy (FE-SEM) analysis (Fig. 6a). The sheet structure of RGO and presence of AC deposited on RGO is observable. Figure 6b is the corresponding selected area electron diffraction (SAED) pattern of this composite matches the result of the X-ray diffraction (XRD) pattern. Figure 6c shows the XRD pattern of this composite. From the low-angle reflection, (001), and the broad in-plane reflections at higher 2θ values by their indices [(020), (110), (130), (200) and (060)] the presence of aminoclay associated with GO can be concluded [9,67]. Figure 6d

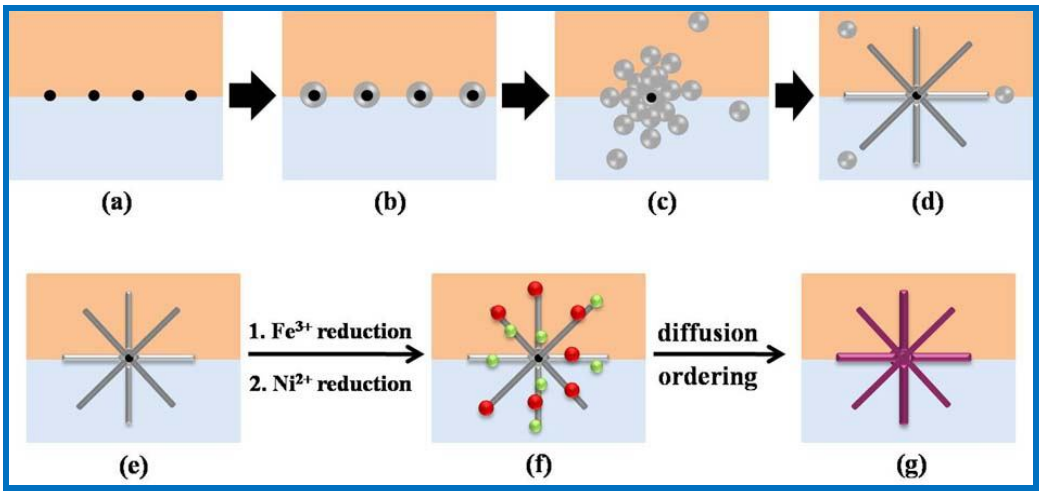

Scheme 2. Steps of formation of $PtPdNiFeFe_2O_3$ tetrametallic alloy nanodendrites [8]

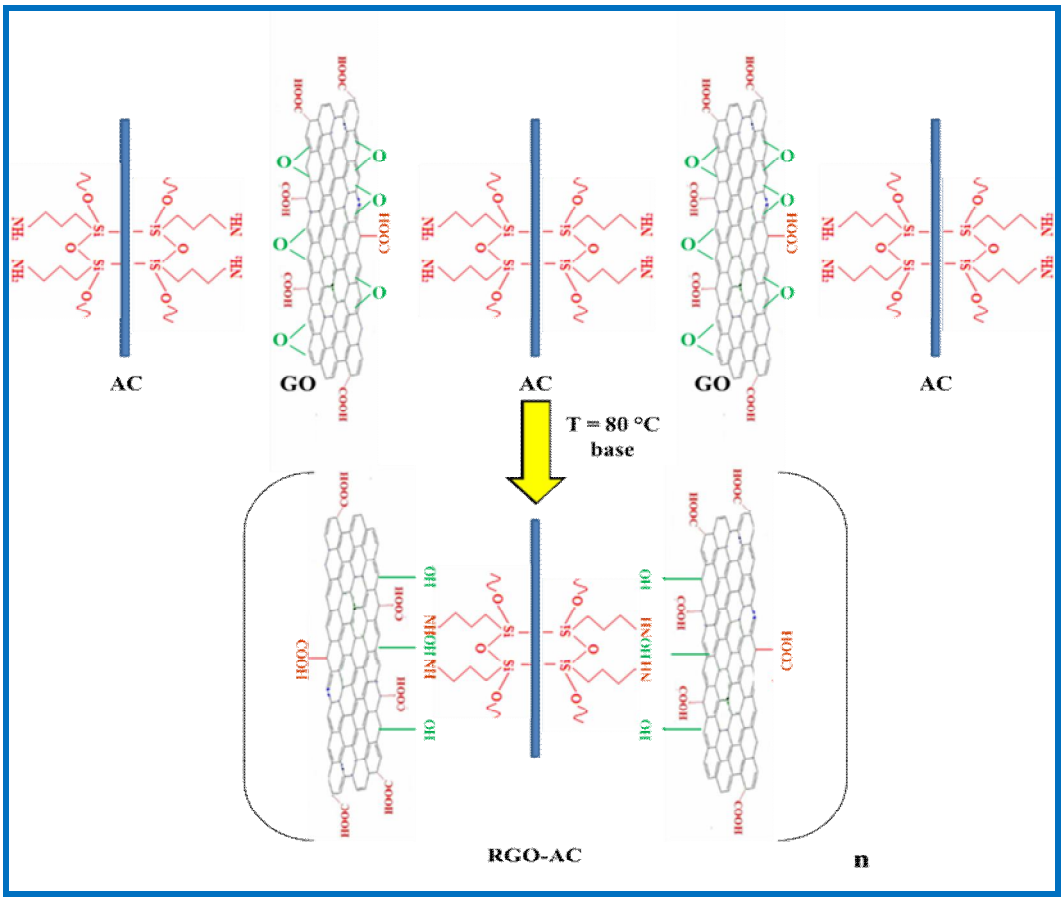

Scheme 3. RGO-AC formation applied as stabilizer for metallic NPs [18]

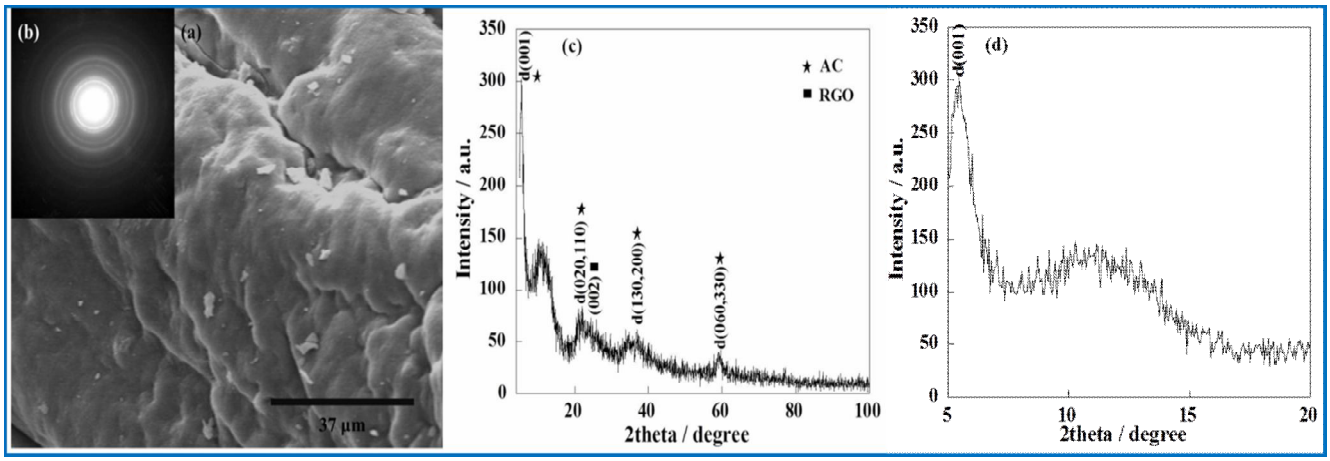

Fig. 6. RGO-AC composite characterization using (a) FE-SEM, (b) SAED, (c) XRD pattern [18] and (d) the low angle range of the XRD pattern.

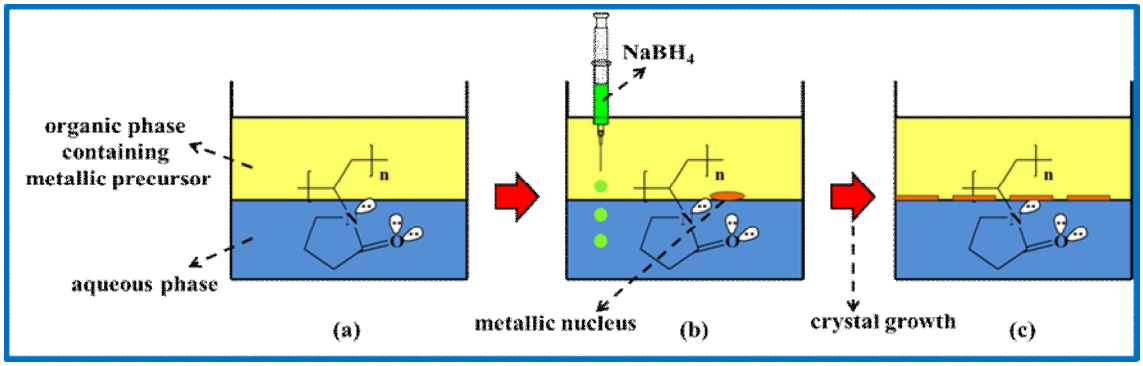

Scheme 4. PVP stabilizes metallic NPs at toluene-water interface [5]

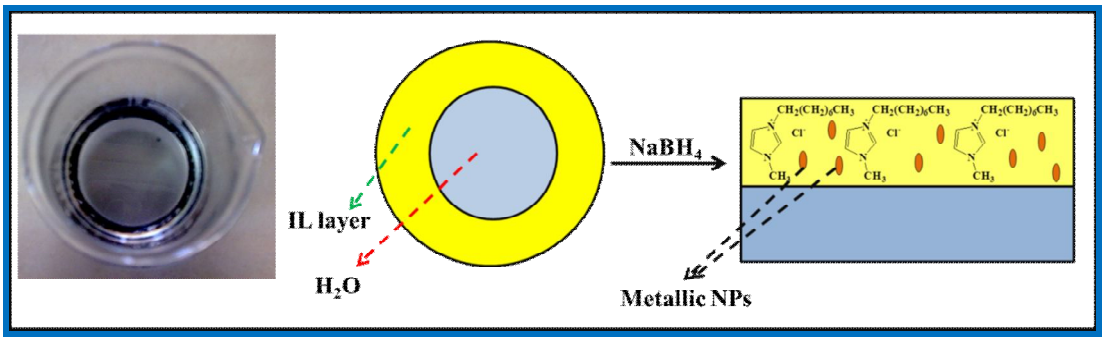

Fig. 7. Stabilization of Pt NPs using [C_8mim][Cl].

exhibits the low angle range of the XRD pattern. Furthermore, the weak and broad peak at the 2θ = 24.2° (002) confirms the GO intercalation with aminoclay and RGO formation after the additional ring-opening reaction between the amine groups of AC and the epoxy group of GO, which means that this peak is attributed to RGO.

Polyvinylpyrrolidone (PVP) is a water-soluble polymer made from the monomer *N*-vinylpyrrolidone and can apply as a stabilizer for metallic NPs (Scheme 4).

ILs with different physical properties such as high charge density, dielectric constant, polarity and supramolecular network formation are potentially good candidates for the formation of stabilized NPs. Stabilization of Pt/Pd NPs from organometallic precursors, [$PtCl_2$(cod)] and [$PdCl_2$(cod)] in the presence of 1-aminoethyl-3-methyl-imidazolium bromide [C_2NH_2mim][Br], 1-methyl-3-octylimidazolium chloride [C_8mim][Cl] and 1-methyl-3-octylimidazolium tetrafluoroborate [C_8mim][BF_4] was investigated. This stabilization is due to the electrostatic and steric properties of ionic liquids in the absence of any additional stabilizers or capping agents (Fig. 7) [68,26,27].

The effects of different stabilizers on the size, morphology and catalytic activity of NPs were investigated by our research group. For Pt nanostructures, in the presence of AC, dendritic structures are produced (Fig. 8a) [5]. In the presence of PVP as a stabilizer, nanosheets of platinum were observed (Fig. 8b) [5]. Spherical NPs are produced in the presence of [C_8mim][Cl], GO and AC-GO (Figs. 8c, d and e [9]). Pt/[C_8mim][BF_4] spherical nanostructures with the mean diameter of 4 nm was formed at the interfaces (Fig. 8h) [27]. In the case of Pd nanostructures, spherical morphology is observable in the presence of GO and AC (Fig. 8f [7], g [18]). Flower-shaped core-shells, spherical and oval-like shapes and spherical Pd nanostructures were obtained in the presence of [C_2NH_2mim][Br], [C_8mim][Cl] and [C_8mim][BF_4], respectively (Fig. 8i-l) [26]. Spherical particles were formed in the presence of β-cyclodextrin (Fig. 8m,n) [28]. Schematic illustration of Pd/β-cyclodextrin thin film formation from [$PdCl_2$(cod)] precursor is shown in Scheme 5. According to this mechanism, (cod) ligand is able to place itself in the β-cyclodextrin porous structure by folding and form a boat conformation (Scheme 5b). Depending on the rate of the addition of a reducing agent, Pd(0) formation may happen *via* routes (c) or (d) (Scheme 5c and d). In liquid-liquid interface method, route (d) was happened due to the low rate of nucleation and growth. Therefore, Pd(0) NPs self-assembled at the interface and Pd/β-cyclodextrin was formed at toluene-water interface.

Furthermore, porous structured metal-organic frameworks can be synthesized from the liquid-liquid interface strategy. Our research group reported the successful synthesis of zeolitic imidazolate framework-8 (ZIF-8) at toluene-water interface with uniform and well-dispersed crystals with rhombic dodecahedral shape and the average side size of 30 nm (Fig. 8o and p) [29]. In the case of bimetallic alloys stabilized on surfaces, for PdCu/RGO the spherical NPs are observable (Fig. 9a) [17]. Figure 9b shows the nanoneedle structure for PtCu/AC [18]. Spherical NPs are the morphology of PtPd and Pt_3Sn nanoalloys stabilized on RGO surface (Figure 9c [25a] and d [10]).

In the case of trimetallic alloys, spherical NPs stabilized on RGO thin layer is observable for PdCuFe/RGO (Figure 10a,b) [14] and PdNiZn/RGO (Fig. 10c) [15] thin films.

Also, covalent attachment of 3-(aminomethyl)pyridine (3-ampy) to GO was investigated to produce a new stabilizer for Pd nanostructures [69]. The N group of the pyridine ring in 3-ampy helps in the uniform and well-organized dispersion of the Pd(0) NPs. Our studies show that the Pd/3-ampy-RGO nanohybrid is suitable for the Suzuki-Miyaura C-C coupling reaction. Preparation of 3-ampy-GO is illustrated in Scheme 6.

Pd nanostructures stabilized on 3-ampy-RGO at liquid-liquid interface was characterized by TEM analysis. Spherical NPs with the mean diameter of 5 nm are the product of this reaction (Fig. 11b). Figure 11a shows the SEM image of the GO support.

Furthermore, Pd NPs were supported on magnetic Fe_3O_4/RGO nanohybrid by reduction of dichloropalladium (II) complex in water medium. Pd/Fe_3O_4/RGO nanohybrid was characterized by TEM (Fig. 12a). Our study shows that this nanohybrid was suitable for Suzuki-Miyaura C-C coupling reaction in environmentally friendly medium of water [70]. The same procedure was continued for Pt NPs (Fig. 12b). Scheme 7 shows the formation of Fe_3O_4/RGO magnetic support.

In another investigation, cyclometallated palladium

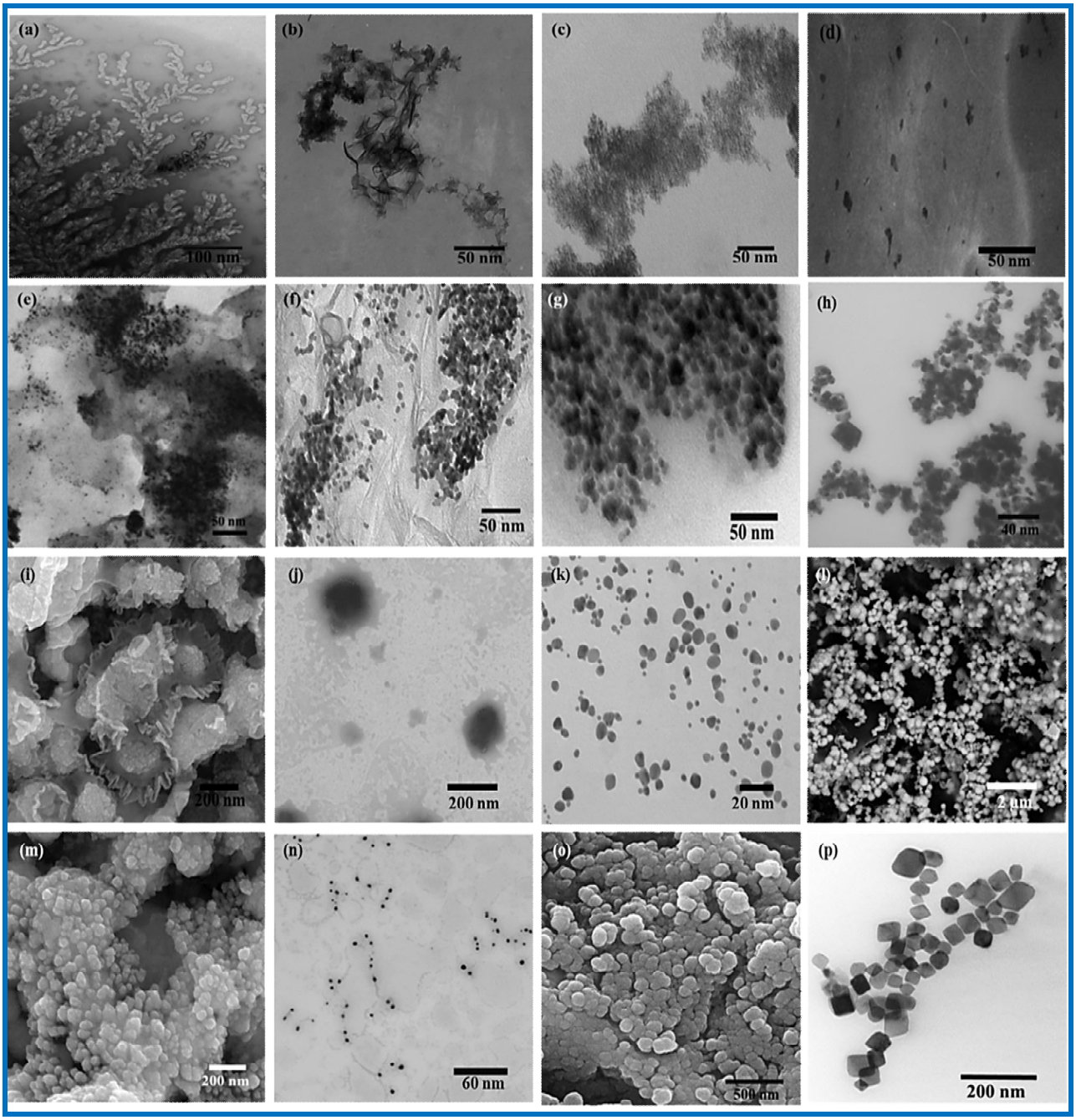

Fig. 8. TEM images of (a) dendritic Pt/AC [5], (b) Pt/PVP nanosheets [5], (c) Pt[C_8mim][Cl] NPs, (d) Pt/RGO NPs [9], (e) Pt/AC-RGO NPs [9], (f) Pd/RGO NPs [7], (g) Pd/AC NPs [18], (h) Pt/[C_8mim][BF_4] spherical nanostructures [27], (i) Pd/[C_2NH_2mim][Br] (SEM image) flower-shaped core-shells [26], (j) Pd/[C_2NH_2mim][Br] core-shells [26], (k) Pd/[C_8mim][Cl] spherical and oval-like shapes [26], (l) Pd/[C_8mim][BF_4] (SEM image) spherical nanostructures [26], (m) Pd/β-cyclodextrin (SEM image) spherical NPs [28], (n) Pd/β-cyclodextrin spherical NPs [28], (o) ZIF-8 (SEM image) [29] and (p) ZIF-8 rhombic dodecahedral structure [29].

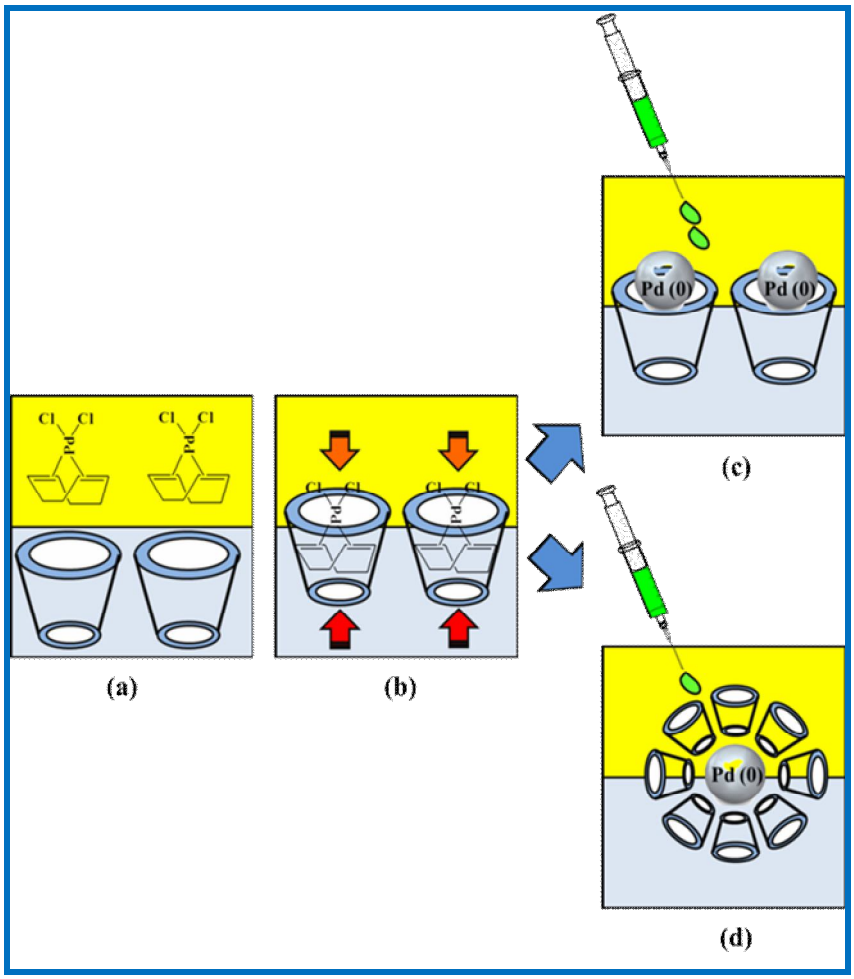

Scheme 5. Pd/β-cyclodextrin thin film synthesis at the interfaces *via* an inclusion complex formation [28]

complexes, [Pd(C^N)Cl(L)], have been synthesized. C^N stands for N(1), C(2′)-chelated deprotonated 2-phenylpyridine and L stands for dimethylsulfoxide (dmso) (complex 1) or (PPh_3) (complex 2) (Scheme 8). Furthermore, covalent bonding of complex 1 onto the GO surface led to the attachment of complex 1 to amine functionalized GO (*f*-GO) which plays enhanced catalytic activity towards Suzuki-Miyaura C-C coupling reaction between aryl halides and phenylboronic acid at 25 °C in comparison to homogeneous catalysts and recovered for several reaction cycles with high yield. Figure 13a exhibits the TEM image of *f*-GO and Figure 13b is related to complex 1-*f*-GO nanohybrid [71].

In another study, new stabilizer was synthesized from silylation process between the organosilane compound ((3-aminopropyl)triethoxysilane (APTES)) and GO (*f*-GO). $[Cu(PPh_3)_3Cl]$ complex was anchored on the GO surface through coordination interaction with organosilane ligand spacers (Scheme 9). The obtained catalyst was characterized by X-ray photoelectron spectroscopy (XPS) (Figure 14), SEM and energy dispersive analysis of X-ray (EDAX) elemental mapping (Fig. 15) and TEM (Fig. 16) analysis. This catalyst exhibited interesting catalytic activity toward Sonogashira reaction of aryl halides and phenylacetylene in aqueous medium with considerable recycling in comparison to homogeneous reaction medium [72].

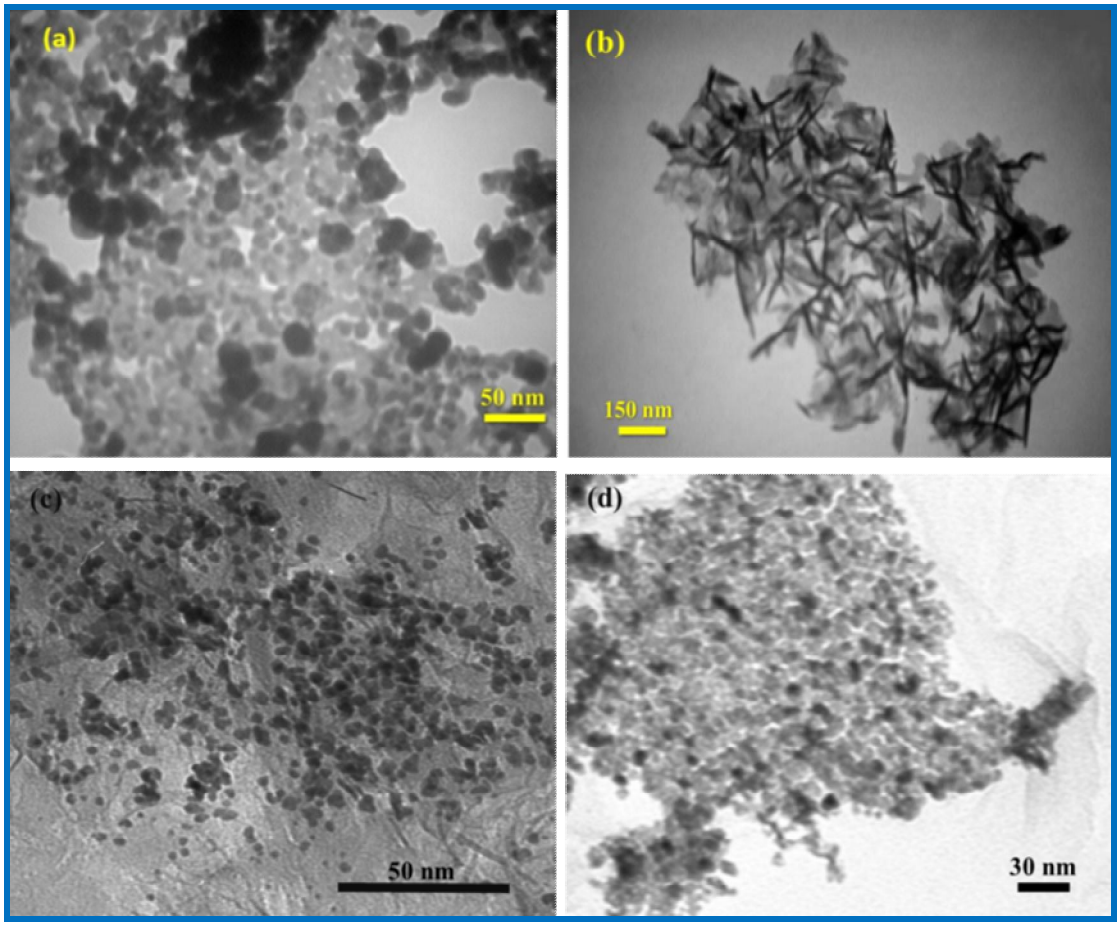

Fig. 9. TEM images of (a) PdCu/RGO [17], (b) PtCu/AC [18], (c) PtPd/RGO [25a] and (d) Pt_3Sn/RGO [10] thin films.

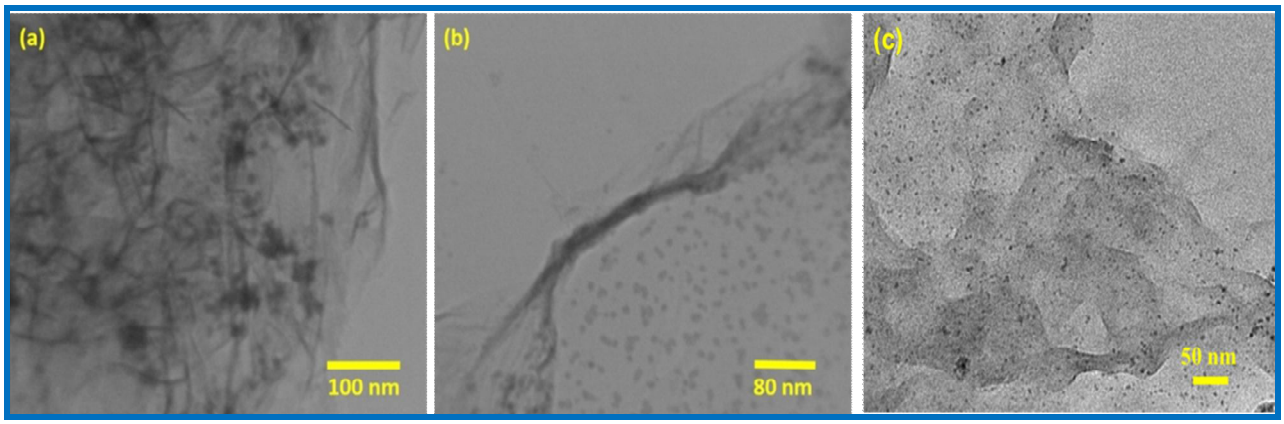

Fig. 10. TEM images of (a,b) PdCuFe/RGO [14] and (c) PdNiZn/RGO [15] thin films.

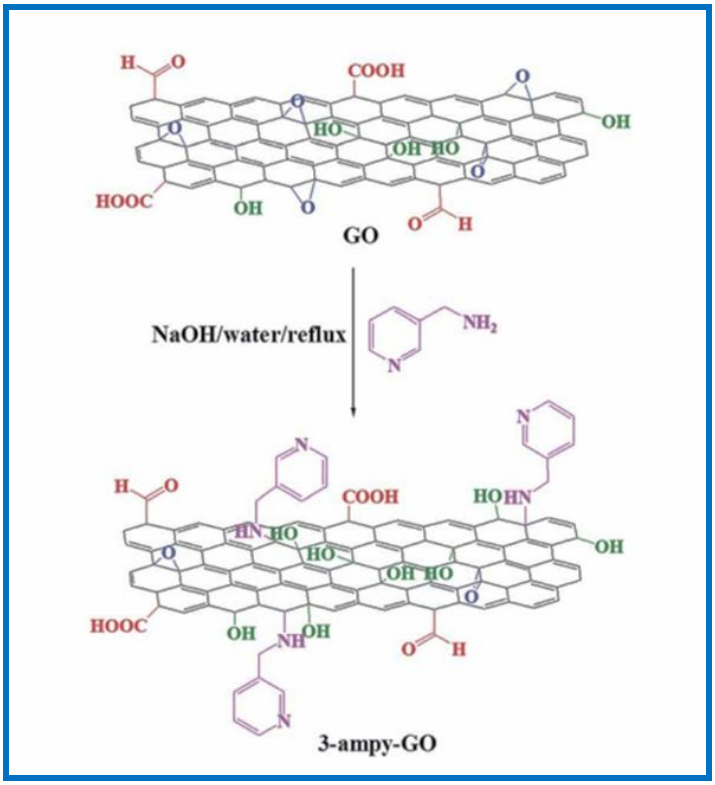

Scheme 6. 3-Ampy-GO formation applied as a support [69]

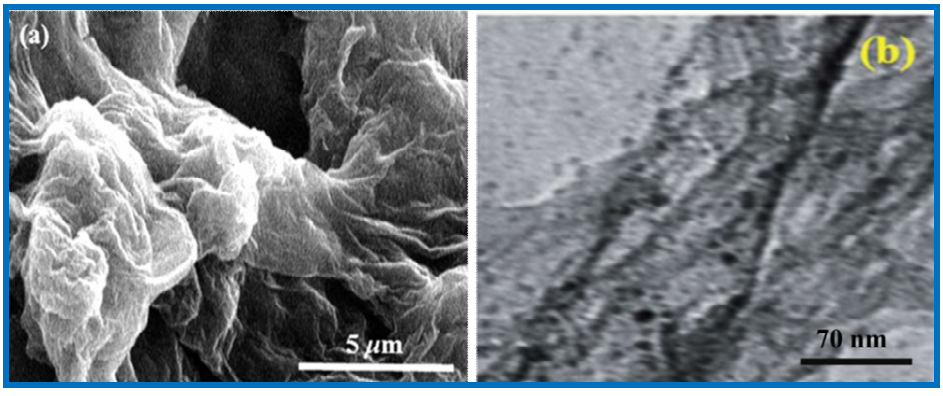

Fig. 11. (a) SEM image of GO and (b) TEM image of Pd/3-ampy-RGO thin film [69].

APPLICATIONS

Application as Electrocatalyst for DMFC

Platinum-based electrocatalysts have been investigated for methanol and ethanol oxidation in direct alcohol fuel cells (DAFCs) as power sources for the near future [73]. But, the high cost and low scarcity of Pt limits the wide application of Pt-based electrocatalysts [74,75]. One of the

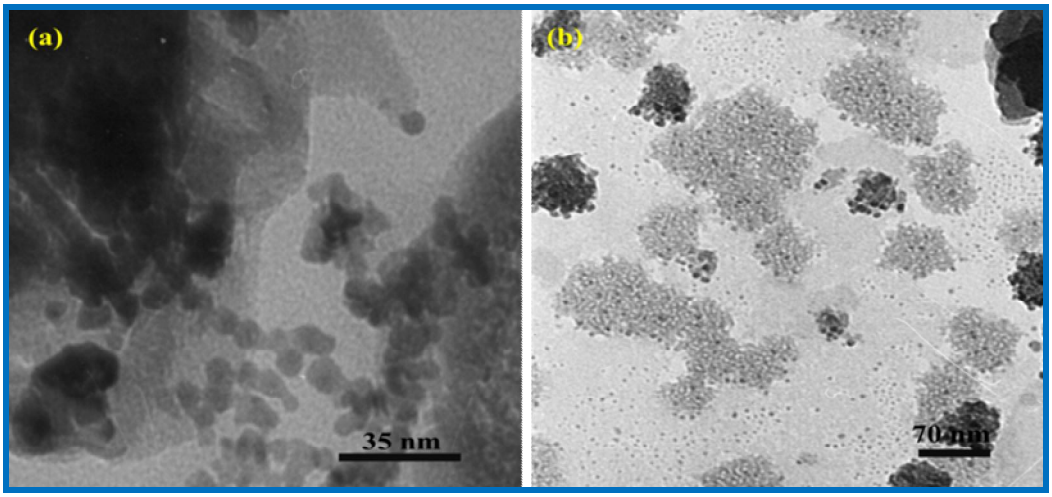

Fig. 12. (a) TEM images of (a) Pd/Fe_3O_4/RGO and (b) Pt/Fe_3O_4/RGO nanohybrid [70].

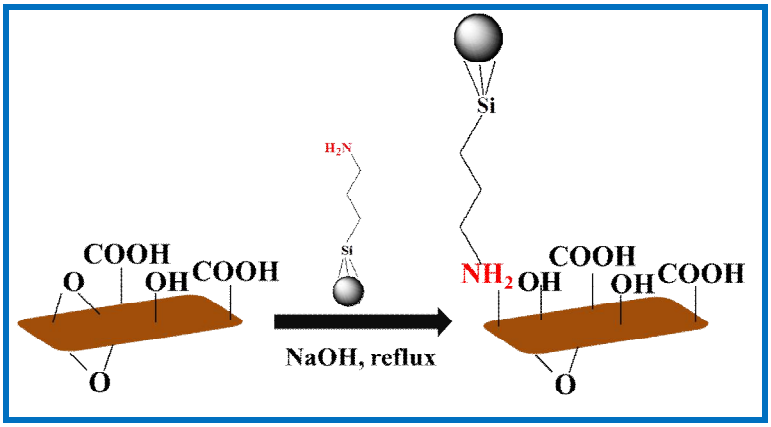

Scheme 7. Preparation of Fe_3O_4/RGO hybrid as a magnetic support [70]

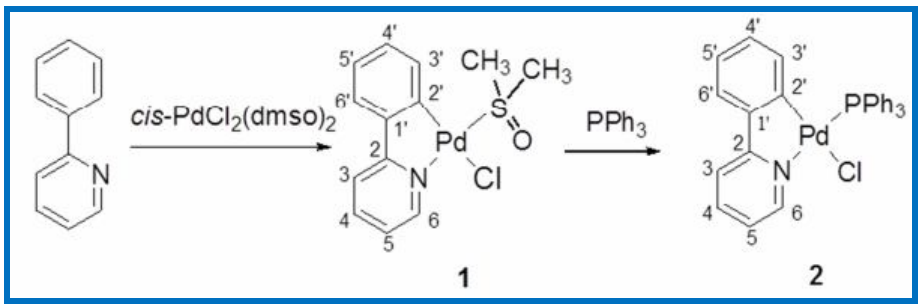

Scheme 8. Steps of cyclometallated palladium complexes formation [71]

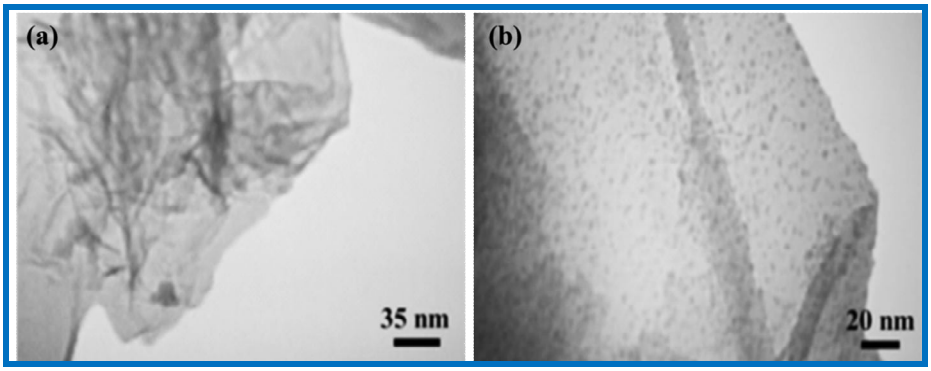

Fig. 13. TEM images of (a) *f*-GO and (b) complex 1-*f*-GO nanohybrid [71].

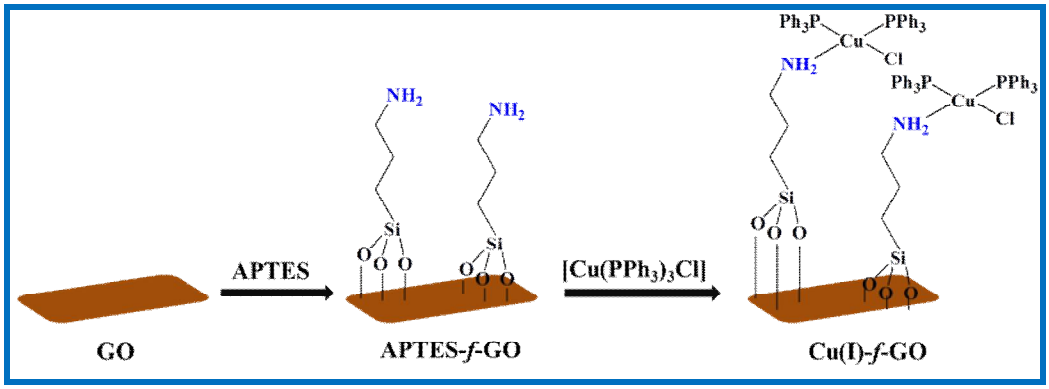

Scheme 9. Cu(I)-*f*-GO nanohybrid formation by anchoring the Cu complex on the *f*-GO surface [72]

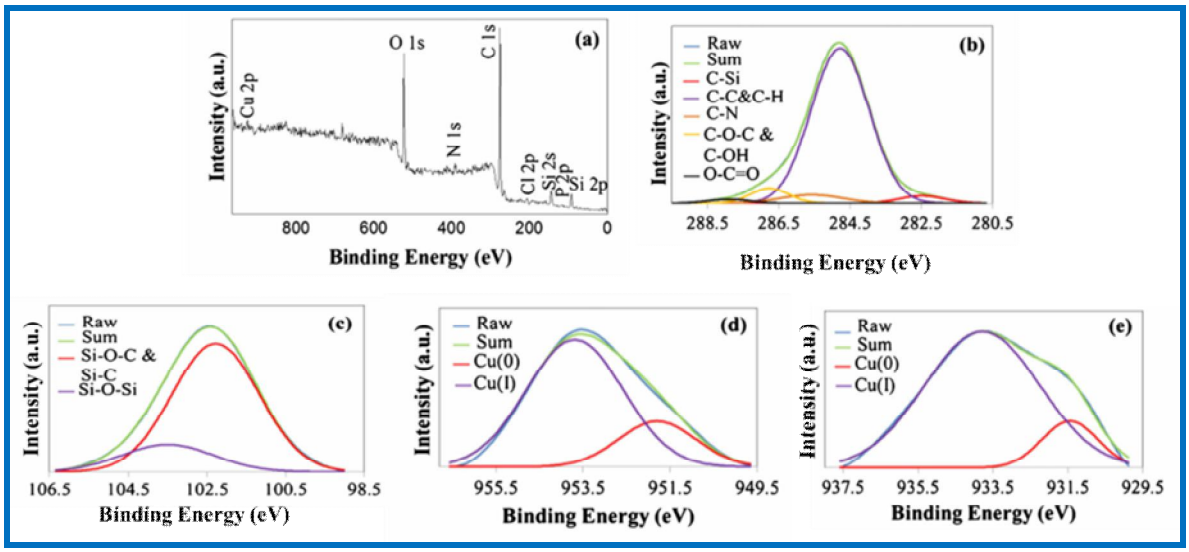

Fig. 14. XPS spectra of the as-synthesized Cu(I)-*f*-GO nanohybrid, (a) the survey curve, (b) C 1 s, (c) Si 2p, (d) Cu $p_{1/2}$ and (e) Cu $p_{3/2}$ [72].

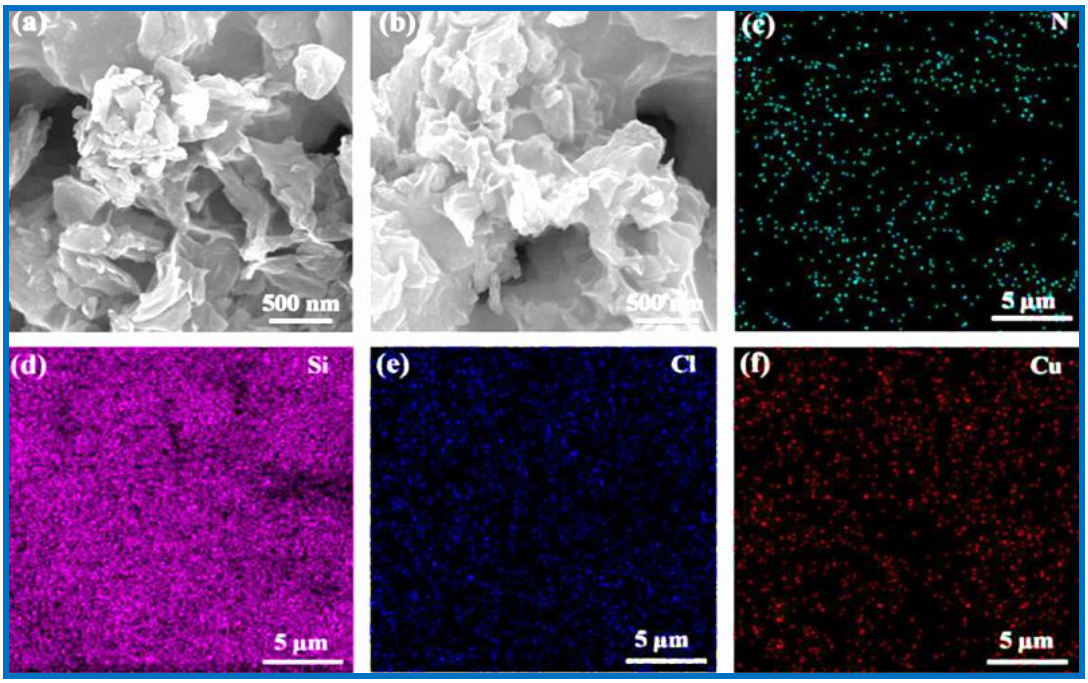

Fig. 15. (a,b) SEM images of the as-synthesized Cu(I)-*f*-GO nanohybrid, and the related EDAX mapping of (c) N, (d) Si, (e) Cl and (f) Cu [72].

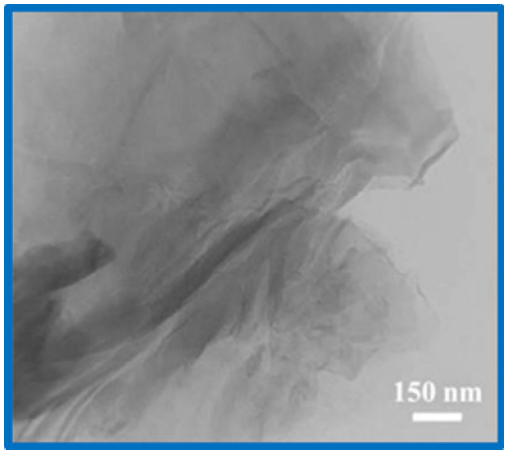

Fig. 16. TEM image of the as-synthesized Cu(I)-*f*-GO nanohybrid [72].

important and considerable topics in the catalysis field is investigating the multimetallic NPs and Pt and Pd-based NPs are more interested due to their higher activity in catalytic reactions especially in fuel cells [76]. To find the effective and less expensive non-Pt electrocatalysts for DAFCs, alloying method is helpful. Electrocatalysts of tri and tetrametallic alloy thin films exhibit considerable catalytic activity for the methanol oxidation reaction (MOR)

in fuel cell anodes. Constructing metallic alloys with special morphology, low cost and improved catalytic activity is one of our main aims. Cyclic voltammograms of the as-prepared nanostructures (monometallic Pt thin films obtained from $[PtCl_2(cod)]$, $[PtI_2(cod)]$ and $[Pt(p\text{-tolyl})_2(SMe_2)_2]$ precursors [6], Pd thin film [25a], stabilized monometallic thin films such as Pt/RGO [9], Pd/RGO [25a], Pt/RGO-AC [9], Pt/ILs [27] and Pd/ILs [26], bimetallic alloys such as PtPd [25a], PtSn [10] and PtNi [8], PtPd/RGO [25a] and Pt_3Sn/RGO [10] thin films, trimetallic PtPdNi [8] and PtZnSn [11] and tetrametallic alloys such as $PtPdNiFeFe_2O_3$ [8], PtPdNiSn [8] and PtPdNiZn [8] thin films) in 0.5 M sulfuric acid at a scan rate of 50 mV s^{-1} (Figs. 17-18a-u) were used to study the catalytic activity of the thin films by investigating the processes of hydrogen adsorption and methanol oxidation on the films. As is obvious, some humps are observable on these diagrams which are belong to atomic hydrogen desorption and adsorption (I and IV regions in Figs. 17a-u). Formation of metal oxide and also reduction was observed at II and III regions in Figs. 17a-u. The electrocatalytic activity of the as-prepared thin films was characterized by cyclic voltammetry in an electrolyte of methanol (0.5 M) and sulfuric acid (0.5 M) at a scan rate of 50 mV s^{-1}. The resulting voltammograms are shown in Figs. 18a-u. From the cyclic voltammograms, we can conclude that Pd thin films show no considerable methanol oxidation, except in the case of Pd/$[C_2NH_2mim][Br]$ [26].

There are three main facts for investigation of the catalytic activity in the MOR that are as following:

(i) Current density (*J*). The peak current densities of the as-prepared thin films are given in Table 1 applying Fig. 18a-u. According to Table 1, the catalytic activity of the ternary PtPdNi alloy thin film is at least 10 times higher than that of the monometallic Pt NP film.

(ii) (J_f/J_b) ratio. The catalysts tolerance toward poisoning with carbon monoxide is evaluated using the ratio of the forward anodic peak current (J_f) to the backward peak current (J_b), J_f/J_b. The higher value means the more tolerance of catalyst from poisoning during MOR [8]. The J_f/J_b ratios for the thin films are given in Table 1. This ratio is higher for all the metallic alloys than those for the ETEK Pt (0.99), another type of commercial Pt/C (0.605), and monometallic Pt NP thin films (1.28) [6].

(iii) Lower voltage for the onset of current attributed to methanol oxidation. This amount is approximately lower for the as-prepared thin films than that for monometallic Pt NP thin film electrode (0.73 V *vs*. NHE). This shift exhibits that these alloy thin films have a positive effect on promoting the methanol oxidation process by lowering the overpotential (Table 1).

All of these results strongly show that the tetra, tri and bimetallic alloy nanostructures and also stabilized thin films exhibit a higher electrocatalytic activity than the monometallic Pt thin film and commercial Pt/C electrocatalyst, due to their higher J_f/J_b ratio. So, more complete methanol oxidation is predictable. It is noteworthy that these electrocatalysts can promote the methanol oxidation by lowering the overpotential.

Why alloys are better electrocatalysts for methanol oxidation? The reasons are as following:

(i) High specific surface areas of the alloys. Recent investigations show that nanostructures with specific geometric shapes and high surface area exhibit high catalytic activity. Noble metal nanocrystals with special morphologies such as thin films, nanosheets and nanodendrites with higher active sites show effective catalytic activity.

(ii) High active sites. The electrocatalytic activities of the as-prepared nanostructures are related to the existence of a high density of low-coordinated atoms in edges and kinks, which are catalytically active sites on their surfaces.

(iii) Synergistic effects. By considering the molecular orbital and band theories and according to the electronic facts it can be concluded that the valance and conduction bands of the metals are changed and electron donation from noble metals such as Pt to some other metals was observed.

A typical cyclic voltammogram recorded for all the as-synthesized thin films in sulfuric acid (0.5 M) and methanol (0.5 M) at different scan rates 20 -100 mV s^{-1}. Figure 19a shows this diagram for Pt thin film as an example. An increase in the current density with the scan rate is observed and the peak potentials nearly show no change (Fig. 19a). Figure 19b shows that the peak current densities are linearly proportional to the square root of the scan rates, suggesting that the electrocatalytic methanol oxidation on these as-prepared alloy thin films is a diffusion-controlled process [6].

Poisoning of Pt-based electrocatalysts surfaces during

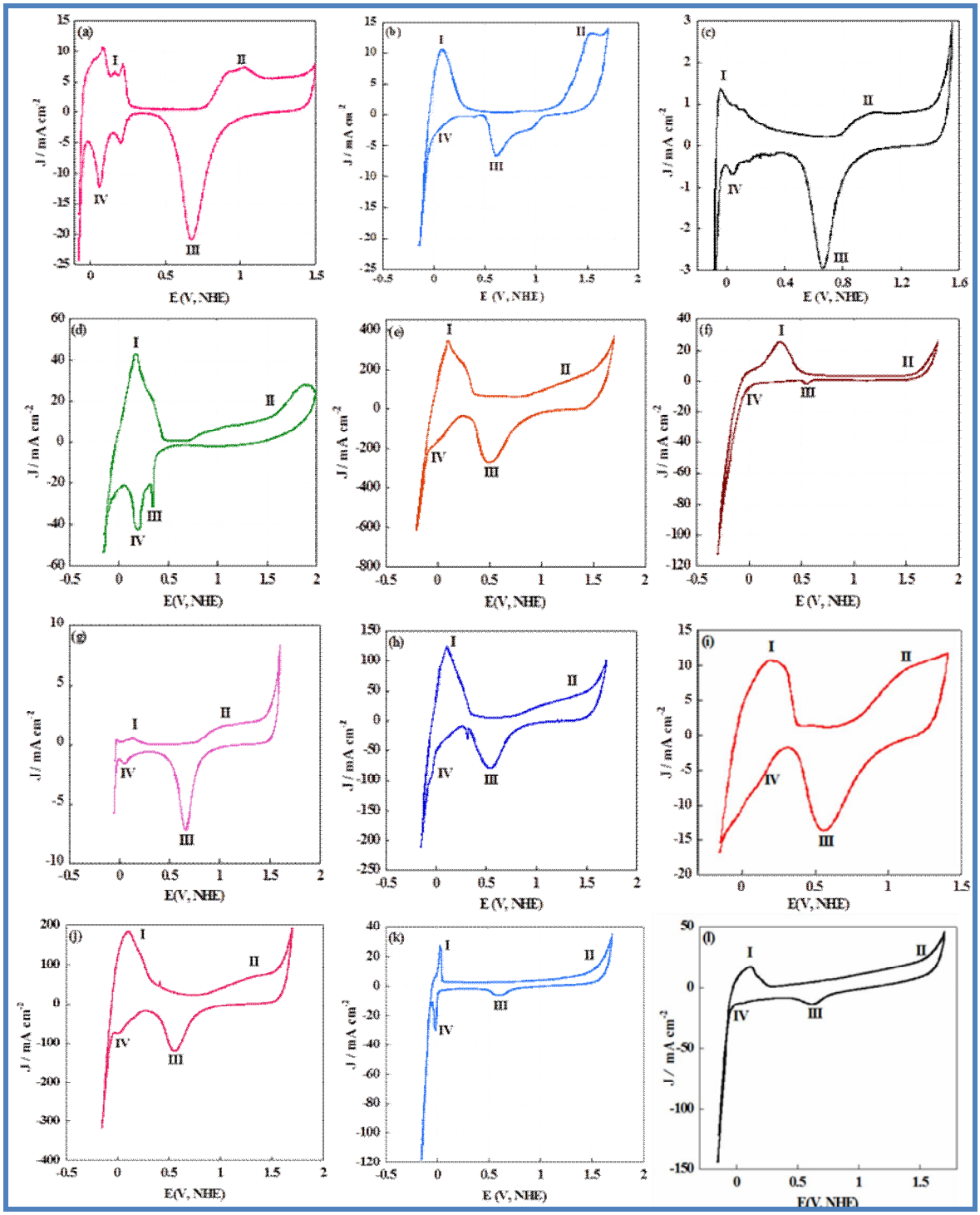

Fig. 17. Cyclic voltammograms of the (a) Pt thin film obtain from [$PtCl_2$(cod)] [6], (b) Pt thin film obtain from [PtI_2(cod)] [6] and (c) Pt thin film obtain from [Pt(*p*-tolyl)$_2$(SMe_2)$_2$] precursors [6], (d) Pd thin film [25a], (e) Pt/RGO [9], (f) Pd/RGO [25a], (g) Pt/RGO-AC [9], (h) PtPd [25a], (i) PtSn [10], (j) PtNi [8], (k) PtPd/RGO [25a], (l) Pt_3Sn/RGO [10], (m) PtPdNi [8], (n) PtZnSn [11], (o) PtPdNiFeFe_2O_3 [8], (p) PtPdNiSn [8], (q) PtPdNiZn [8], (r) Pt/[C_8mim][BF_4] [27], (s) Pd/[C_2NH_2mim][Br] [26], (t) Pd/[C_8mim][Cl] [26] and (u) Pd/[C_8mim][BF_4] [26] thin films in 0.5 M sulfuric acid electrolyte with a scan rate of 50 mV s^{-1}.

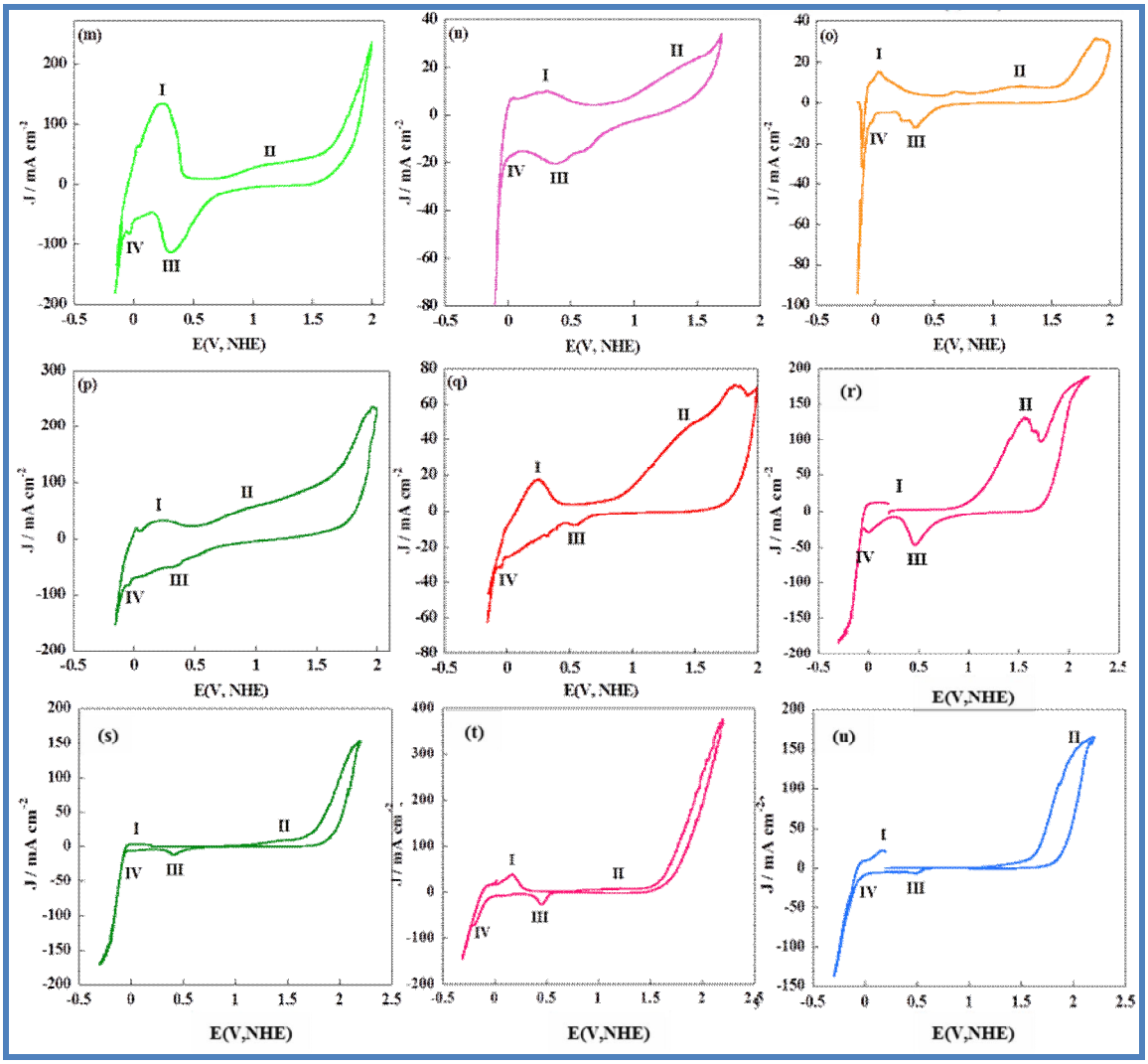

Fig. 17. Continued.

the MOR (Scheme 10) and the oxidation mechanism (Eqs. (5)-(12)) are as following [27]:

$$Pt + CH_3OH \longrightarrow Pt\text{-}CH_3O + H^+ + e^- \quad (5)$$

$$Pt\text{-}CH_3O \longrightarrow Pt\text{-}CH_2O + H^+ + e^- \quad (6)$$

$$Pt\text{-}CH_2O \longrightarrow Pt\text{-}CHO + H^+ + e^- \quad (7)$$

$$Pt\text{-}CHO \longrightarrow Pt\text{-}CO + H^+ + e^- \quad (8)$$

$$Pt\text{-}OH_2 \longrightarrow Pt\text{-}OH + H^+ + e^- \quad (9)$$

$$Pt\text{-}OH \longrightarrow Pt\text{-}O + H^+ + e^- \quad (10)$$

$$Pt\text{-}CO + Pt\text{-}O \longrightarrow CO_2 \quad (11)$$

The overall reaction is:

$$CH_3OH + H_2O \longrightarrow CO_2 + 6H^+ + 6e^- \quad (12)$$

The application of PtFe nanostructures in

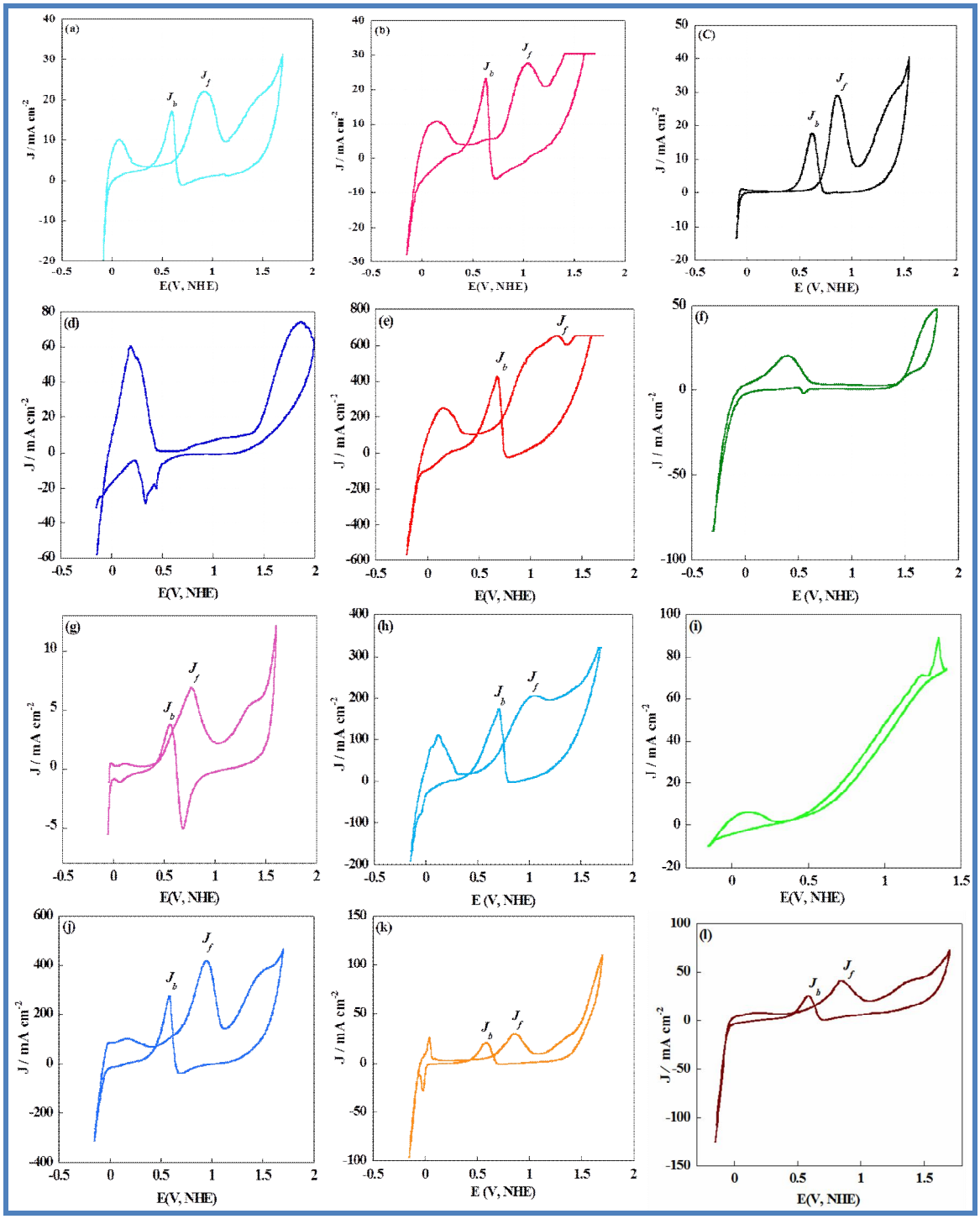

Fig. 18. Cyclic voltammograms of the (a) Pt thin film obtain from [$PtCl_2$(cod)] [6], (b) Pt thin film obtain from [PtI_2(cod)] [6] and (c) Pt thin film obtain from [Pt(*p*-tolyl)$_2$(SMe_2)$_2$] precursors [6], (d) Pd thin film [25a], (e) Pt/RGO [9], (f) Pd/RGO [25a], (g) Pt/RGO-AC [9], (h) PtPd [25a], (i) PtSn [10], (j) PtNi [8], (k) PtPd/RGO [25a], (l) Pt_3Sn/RGO [10], (m) PtPdNi [8], (n) PtZnSn [11], (o) PtPdNiFeFe_2O_3 [8], (p) PtPdNiSn [8], (q) PtPdNiZn [8], (r) Pt/[C_8mim][BF_4] [27], (s) Pd/[C_2NH_2mim][Br] [26], (t) Pd/[C_8mim][Cl] [26] and (u) Pd/[C_8mim][BF_4] [26] thin films in 0.5 M sulfuric acid electrolyte containing 0.5 M CH_3OH with a scan rate of 50 mV s^{-1}.

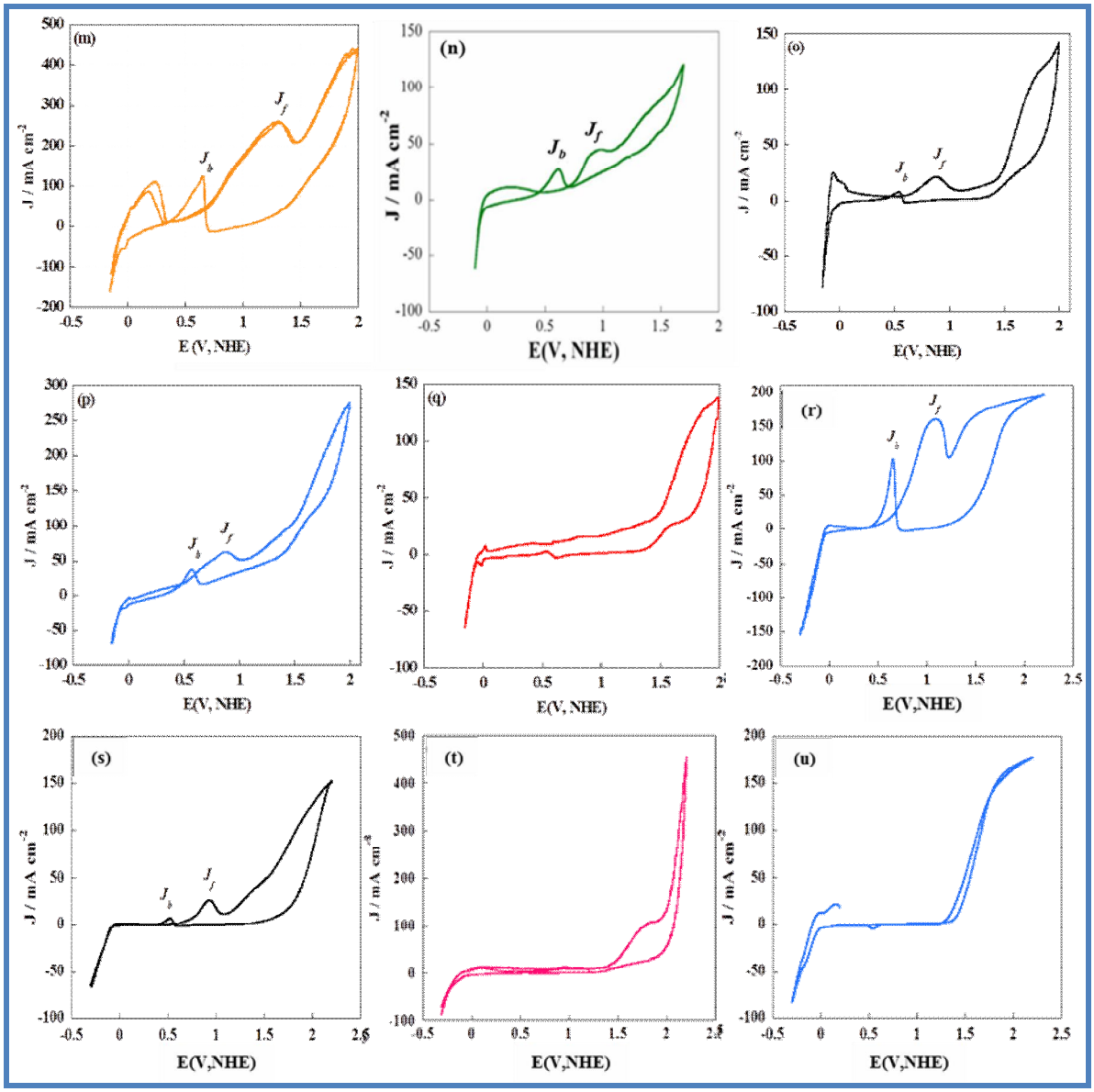

Fig. 18. Continued.

electrocatalytic processes limited due to their hard synthesis. High temperature used for this synthesis caused severe problems such as aggregation and wide size distribution of NPs [12]. Our research group could synthesize $PtFeFe_2O_3$ alloy thin film *via* a simple procedure and use it as an electrocatalyst in MOR (Scheme 11) [12].

MOR on the $PtFeFe_2O_3$ thin film in alkaline medium was investigated. Choosing the alkaline medium is due to the solubility of Fe_2O_3 in acidic medium. Cyclic voltammogram of $PtFeFe_2O_3$ NPs thin film in NaOH (0.5 M) and methanol (0.5 M) at a scan rate of 50 mV s^{-1} is shown in Fig. 20. The J_f/J_b ratio is about 8.09. The number of exchanged electrons can be calculated from the following equations (13-14) in the case of an irreversible electrochemical reaction during MOR [84]:

Table 1. Comparison of Different Electrocatalysts

Electrode	J_f/J_b	Current density (mA cm^{-2})	E (V, NHE)	Ref.
Pt thin film[a]	1.28	35.0	0.73	[6]
Pt thin film[b]	1.20	30.4	0.75	[6]
Pt thin film[c]	1.60	40.5	0.65	[6]
Pd thin film	-	74.3	1.38	[25a]
Pt/RGO thin film	1.55	663.2	0.54	[9]
Pd/RGO thin film	-	47.4	1.42	[25a]
Pt/RGO-AC thin film	1.82	12.1	0.34	[9]
PtPd thin film	1.19	321.2	0.54	[25a]
PtSn thin film	-	87.9	0.40	[10]
PtNi thin film	1.52	461.0	0.47	[8]
PtPd/RGO thin film	1.50	110.4	0.63	[25a]
Pt_3Sn/RGO thin film	1.59	73.1	0.55	[10]
PtPdNi thin film	2.08	443.4	0.52	[8]
PtZnSn thin film	1.65	122.0	0.65	[11]
$PtPdNiFeFe_2O_3$ thin film	2.85	144.0	0.59	[8]
PtPdNiSn thin film	1.71	278.0	0.49	[8]
PtPdNiZn	3.50	140.0	0.58	[8]
Commercial Pt/C	0.57	-	-	[77]
Pt/C	0.60	-	-	[78]
Pt/C	1.18	-	-	[79]
PtRu/XC-72[d]	1.05	-	-	[80]
$PtFe_3O_4/CeO_2$	1.32	-	-	[81]
PtAu	1.23	-	-	[82]
ETEK Pt[e]	0.99	-	-	[83]
$PtFeFe_2O_3$ thin film	8.09	105.8	1.53	[12]
Pd/[C_2NH_2mim][Br] thin film	3.72	153	0.55	[26]
Pd/[C_8mim][Cl] thin film	-	454	1.30	[26]
Pd/[C_8mim][BF_4] thin film	-	178	1.25	[26]
Pt/[C_2NH_2mim][Br] thin film	4.54	81.14	0.6	[27]
Pt/[C_8mim][Cl] thin film	3.90	157.57	0.63	[27]
Pt/[C_8mim][BF_4] thin film	1.56	196.24	0.43	[27]
ZIF-8 thin film[f]	-	32.7	-	[29]

[a]Pt thin films obtained from [$PtCl_2$(cod)], [b][PtI_2(cod)] and [c][Pt(*p*-tolyl)$_2$(SMe_2)$_2$] precursors, [d]XC-72: vulcan XC-72 carbon black, [e]commercial Pt-Ru/C catalyst, [f]in alkaline medium.

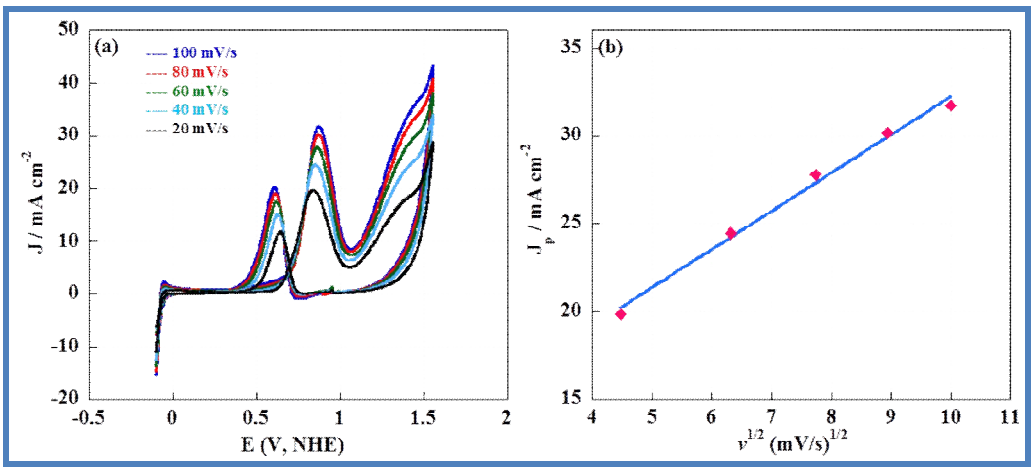

Fig. 19. Cyclic voltammograms of the monometallic Pt thin film at different scan rates in sulfuric acid (0.5 M) and methanol (0.5 M), (b) Dependence of the peak currents on the square root of the scan rates [6].

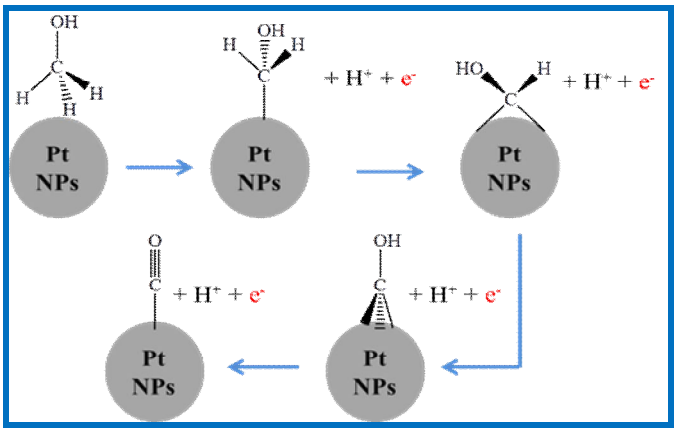

Scheme 10. CO poisoning effect on the Pt electrocatalyst surface [27]

$$E_p - E_{p/2} = 47.7\ (\text{mV})/\alpha n_\alpha \quad (13)$$

$$I_p = (2.99 \times 10^5) n A C_O^* D_O^{1/2} (\alpha n_\alpha)^{1/2} v^{1/2} \quad (14)$$

Using the above equations, the number of exchanged electrons is 6 and confirms this claim that the MOR is an overall 6 electron process (Eq. (12)).

Application as Catalyst in C-C Coupling Reaction

The coupling reaction between aryl boronic acid and aryl halide in the presence of Pd(0) complexes as catalyst can lead to the formation of biaryl compounds with pharmaceutical, polymer and material applications [85]. General conditions for these kinds of reactions are the presence of Pd/ligand complexes in the toxic medium of organic solvents [85]. Finding effective and environmentally friendly catalysts with low Pd dosage is a challenge. Recently, we have made Pd-based bimetallic NP thin film catalysts, such as Pd-Cu [17] and Pd-Zn [19], that exhibit higher catalytic activity in Suzuki-Miyaura reaction compare to monometallic Pd thin film NPs [7] and other Pd-based complexes. Pd/β-cyclodextrin [28] and Pd/ILs [26]

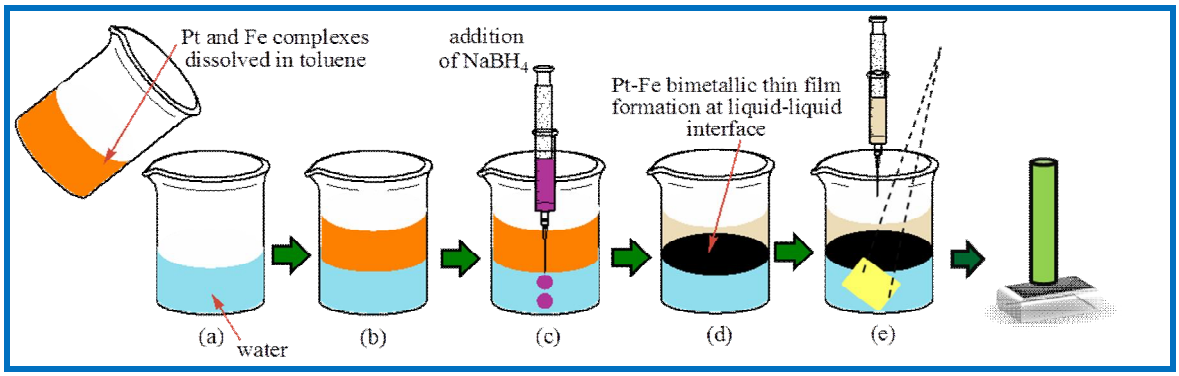

Scheme 11. Formation of the $PtFeFe_2O_3$ bimetallic NPs thin film at liquid-liquid interface from a facile strategy and transfer to a glassy carbon electrode for electrocatalytic applications [12]

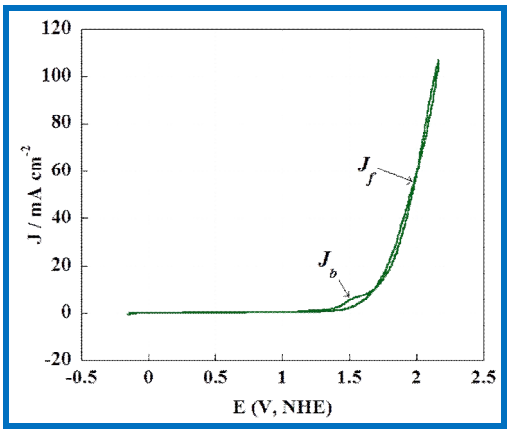

Fig. 20. Cyclic voltammogram of $PtFeFe_2O_3$ thin film in NaOH (0.5 M) electrolyte containing CH_3OH (0.5 M) with a scan rate of 50 mV s^{-1} [12].

thin films showed interesting catalytic activity. The catalytic activity of the as-synthesized catalysts for the coupling reaction of phenylboronic acid and bromobenzene is illustrated in Table 2.

Compared to classical reactions, these catalysts have the considerable advantages such as applying green solvent, short reaction times, low catalyst loading and cost, reusability of the catalyst without considerable loss of catalytic activity, presence of all atoms on the surface, high active sites and high yields with unactivated aryl halides.

One of the useful strategies for the synthesis of organic compounds is Sonogashira cross-coupling reaction. The organic synthesis such as construction of C-C bonds between terminal alkynes and vinyl/aryl halides is very important [92-94]. The reaction products have wide applications for the synthesis of various drugs, nanomaterials and natural products [95]. In general, palladium catalysts progress the Sonogashira cross-coupling reactions by using copper salt as cocatalyst and an amine base. Owning to their high cost, difficult reusability and pollution, the palladium-free Sonogashira coupling reaction has been attracting universal interest [96,97]. So, finding a modified catalytic strategy for the cross coupling reaction of alkynes with aryl halides and replacing palladium with non-

Table 2. Catalytic Performance of Different Pd-based Catalysts in the Coupling of Phenylboronic Acid and Bromobenzene

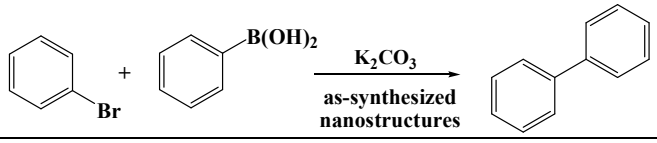

Entry	Catalyst	Solvent	Base	Temp (ºC)	Time (h)	Yield (%)	Ref.
1	PdNi NPs	(H_2O/EtOH[a] 1:1)	K_2CO_3	50	7	65	[86]
2	Pd/SBA-15[b]	(H_2O/EtOH 1:3)	K_2CO_3	85	10	88	[87]
3	Pd/SiO_2/TEG[c]	toluene	K_3PO_4	110	12	86	[87]
4	Pd-G-3[d]	EtOH	NaOAc[e]	Reflux	24	42	[87]
5	Pd NPs	Ionic liquid[f]	NBu_4OH[g]	60	1.5	93	[87]
6	PdCu	H_2O	K_2CO_3	80	1.33	87	[17]
7	PdCu/RGO	H_2O	K_2CO_3	80	0.5	87	[17]
8	Pd_1Ni_2	DMF[h]	NaOH	140	10	93.8	[88]
9	Pd/Fe_3O_4 NPs	MeOH[i]	K_3PO_4	60	18	95	[89]
10	Pd-Ni/Fe_3O_4	EtOH	K_2CO_3	80	0.5	95	[85]
11	Pd thin film	H_2O	K_2CO_3	80	1.5	90	[7]
12	Pd/RGO thin film	H_2O	K_2CO_3	80	0.5	95	[7]
13	PtPdCu	H_2O	K_2CO_3	80	0.42	94	[17]
14	PdZn thin film	(H_2O/EtOH 1:1)	K_2CO_3	80	1	94	[19]
15	PdPtZn thin film	H_2O-CTAB[j]	K_2CO_3	80	0.75	96	[19]
16	Diimine/Pd(II)	DMA[k]	K_2CO_3	80	1	58	[90]
17	NHC-Pd[l]	EtOH	K_3PO_4	Reflux	0.5	75	[91]
18	PdNiZn	H_2O	K_2CO_3	80	0.25	90	[15]
19	PdNiZn/RGO	H_2O	K_2CO_3	80	0.16	97	[15]
20	Pd/3-ampy-RGO	(H_2O/EtOH 1:1)	K_2CO_3	80	0.5	85	[69]
21	Pd/Fe_3O_4/RGO	H_2O	K_2CO_3	80	0.42	97	[70]
22	Cyclometallated Pd-*f*-GO	Toluene	K_2CO_3	r.t.	0.5	90	[71]
23	Pd/CdS	H_2O	K_2CO_3	r.t. (sun light)	1	94	[16]
24	Pd/[C_2NH_2mim][Br] thin film	H_2O	K_2CO_3	r.t.	0.33	70	[26]
25	Pd/[C_8mim][Cl] thin film	H_2O	K_2CO_3	r.t.	0.66	95	[26]
26	Pd/[C_8mim][BF_4] thin film	H_2O	K_2CO_3	r.t.	0.5	70	[26]
27	Pd/[C_2NH_2mim][Br] thin film	H_2O	K_2CO_3	r.t./ultrasonic waves	0.33	80	[26]
28	Pd/[C_8mim][Cl] thin film	H_2O	K_2CO_3	r.t./ultrasonic waves	0.25	97	[26]
29	Pd/[C_8mim][BF_4] thin film	H_2O	K_2CO_3	r.t./ultrasonic waves	0.5	97	[26]
30	Pd/β-cyclodextrin	H_2O	K_2CO_3	r.t.	0.2	97	-

[a]EtOH: ethanol; [b]SBA-15: Santa Barbara amorphous type silica; [c]TEG: tetra(ethylene glycol); [d]generation-3 palladium NP-cored dendrimer; [e]NaOAc: sodium acetate; [f]tetraalkylammonium-based ionic liquids; [g]tetrabutylammonium hydroxide; [h]DMF: dimethylformamide; [i]MeOH: methanol; [j]CTAB: cetyltrimethylammonium bromide; [k]DMA: dimethyl acetamide; [l]NHC: N-heterocyclic carbene.

precious, environmentally friendly and abundant metals is important [98]. Using transition metal NPs as catalysts in organic synthesis has a significant advantage due to their unique structures and high surface area comparing with the bulk metals [99]. The as-prepared nanostructures were employed as efficient and non-precious catalysts in the Sonogashira coupling reactions (Table 3).

Catalyst for Reduction of *p*-Nitrophenol and Dye Degradation

***p*-Nitrophenol reduction.** ne of the most toxic refractory water pollutants are nitrophenol derivatives. In general, 4-nitrophenol (4-NP) compounds cause severe environmental and water pollution that hampers the public health, causing alteration in the habitat and perturbations in aquatic life [85]. Different strategies were examined for the removal of these pollutants; but reduction of the nitro group seems to be a better strategy. 4-aminophenol (4-AP) is the reduction product of 4-NP, that is a useful organic compound with wide applications [85]. Producing an efficient and recoverable catalyst for 4-NP reduction is already a challenging task. Noble metal nanostructures such as Pd and Pt have been widely used as catalysts in a variety of important fields such as C-C cross-couplings, fuel cells and hydrogenation reactions owing to their excellent catalytic activity and stability [104]. Also, several noble metal catalysts such as Pt, Pd, Rh and Au have been applied for the reduction of 4-NP to 4-AP in the presence of $NaBH_4$ [105,106]. Pal *et al*. have been used coinage metals (Ag, Au and Cu) for the catalytic reduction of aromatic nitro compounds [107]. Nevertheless, using these metal NPs has been limited due to their high cost and scarcity. Both of the reactant (4-NP) and the product (4-AP) have remarkable UV-Vis absorption peaks in basic solution and this leads to simple monitoring of the progress of reduction reactions [5]. Herein, the as-prepared nanocatalysts were used for hydrogenation of nitroaromatic compounds (Scheme 12). Heterostructured nanocatalyst of graphene-supported transition metals prepared by the liquid-liquid interfacial technique exhibited economically catalytic systems for hydrogenation reactions and we hope that they can be applied for other catalytic applications [18].

The reduction or hydrogenation of nitroaromatics led to produce aromatic amines, which have a key role in various fields, such as pharmaceuticals, chemical, or dye industries [18]. The catalytic activities were ascertained by using a UV-Vis spectrometer. Totally, 4-NP shows an original absorption peak centered at 317 nm and shifted to 400 nm in the presence of $NaBH_4$ solution, indicating the formation of the sodium 4-nitrophenolate ions (Fig. 21). The reduction of 4-NP to 4-AP did not show any remarkable progress in the presence of just $NaBH_4$, confirming that the reduction reaction is catalyzed by thin film nanocatalysts.

Addition or formation of a thin film decreases the 400 nm absorption peak and increases the 300 nm absorption peak intensity which is belong to the formation of 4-AP. This investigation can be followed using UV-Vis spectroscopy (Fig. 22). UV-Vis absorption spectra of the reduction of 4-NP was recorded every 30/60 second and the pseudo first-order kinetics can be used to evaluate the rate constants of these reactions. The concentration of $NaBH_4$ is very high, therefore it can be considered constant during the reaction. Also, the absorbencies at λ = 400 nm were collected with time (Fig. 22) and the apparent rate constants were listed in Table 4. The proposed mechanism for the reduction of 4-NP on the surface of catalyst is given in Scheme 13 with complete details. Investigations show that *p*-nitrophenolate adsorption on the catalyst surface, generation of active hydrogen atoms and the rate of charge transfer are important facts that affect the reaction rate.

These facts can affect the catalytic activity:

(i). Stabilization of metal NPs on support surface. Formation of the interface between the two phases leads to adsorption and interaction between GO and reduced-metal precursor that leads to the formation of nanostructures at the interface by self-assembly. Stabilizing nanostructures on the GO surface in the form of thin films can increase the surface area and available active sites. GO with its hydrophobic and hydrophilic functional groups can stabilize aqueous-organic interfaces. Also functional groups can provide the anchoring sites for the metal NPs. Scheme 14 shows the reaction details.

(ii). Alloying effects and morphology. Alloying of metal NPs leads to a higher catalytic activity owing to synergistic effects between the individual metal NPs. Formation of multi-metallic catalysts by the addition of Cu, Ni or Co to Pt, leads to increase the surface to volume ratio and synergistic effects between two metals. These alloy

Table 3. The Sonogashira Coupling Reaction of Iodobenzene with Phenylacetylene

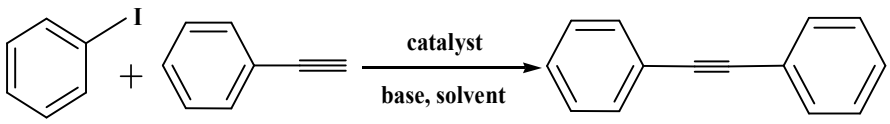

Entry	Catalyst	Solvent	Base	Temp. (°C)	Time (min)	Yield (%)	Ref.
1	PdCu/RGO thin film	H_2O/CTAB	KOH	60	14	95	[14]
2	PdCuFe/RGO thin film	H_2O/CTAB	KOH	60	10	95	[14]
3	Cu(I)-*f*-GO	H_2O	K_2CO_3	80	46	90	[72]
4	$[Cu(PPh_3)_3Cl]$	H_2O	K_2CO_3	80	70	85	[72]
5	Thiospinel $CuCo_2S_4$[a]	H_2O	K_2CO_3	r.t.	35	93	[100]
6	Thiospinel $CuCo_2S_4$/RGO[a]	H_2O	K_2CO_3	r.t.	20	96	[100]
7	Pd/C	Piperidine	Piperidine	100	360	61	[101]
8	Pd/C	DMA	Pyrrolidine	100	360	77	[101]
9	Pd-$CuFe_2O_4/SiO_2$	DMA	1,4-Diazabicyclo[2.2.2]octane	50	1440	80	[102]
10	MMT[b]/Pd-Cu	Ethanol	K_2CO_3	65	960	97[c]	[103]

[a]This catalyst was also synthesized by our research group, [b]MMT: Montmorillonite, [c]In the presence of 2 mol% PPh_3.

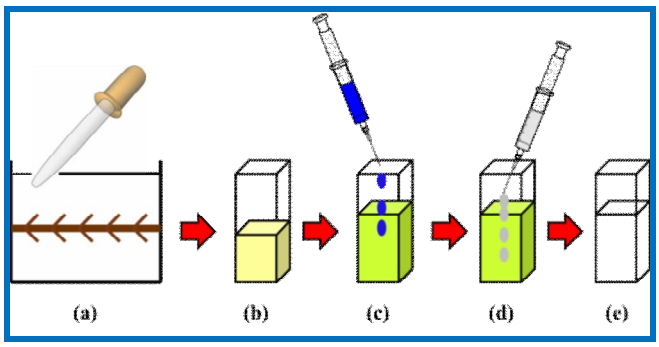

Scheme 12. Details of UV-Vis measurements using catalyst thin films [18]

nanostructures exhibited higher catalytic activity comparing with monometallic Pt NPs.

(iii). Liquid-liquid interface method. Simple and inexpensive liquid-liquid interface strategy provides a significant route for fabrication of high quality nanostructured thin films with high catalytic performances.

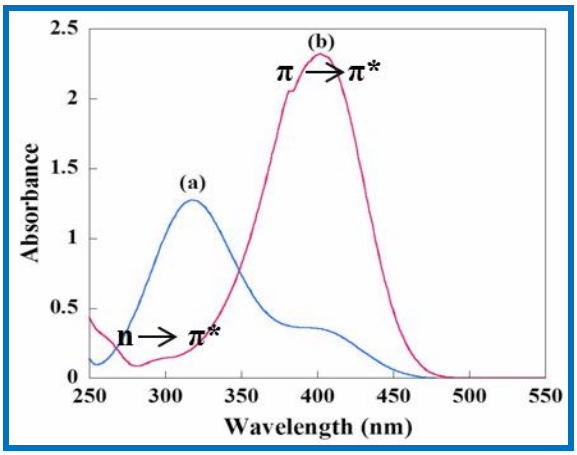

Fig. 21. UV-Vis spectra of (a) aqueous solution of 4-NP, (b) 4-nitrophenolate formation in the presence of $NaBH_4$ [18].

Dye degradation. In order to decrease the water pollution of textile industries with a large amount of toxic non-biodegradable effluents, an efficient method is required for safe extracting the harmful pollutants. Our research group investigated the degradation of azo dyes catalyzed by NPs thin films in the presence of $NaBH_4$. We report *insitu* degradation of methyl orange (MO) by using Pt/Pd-based thin films that monitored by UV-Vis spectroscopy. We have synthesized different thin films from Pt and Pd organometallic precursors in the MO medium (dye degradation and NPs formation is happened simultaneously) and activity of these films were compared in the complete degradation of MO and methyl red (MR) dyes. Also, the rate constants have been determined for the catalyzed reactions. PtPd NPs thin film has shown the highest rate constant for the degradation of MO within only a few seconds due to its well-ordered structure. Furthermore, the effect of presence of MO on the morphology of NPs was investigated. Although different metals and metal alloy thin films obtain from liquid- liquid interface were investigated as the catalysts in the reduction of 4-NP [5,18], C-C coupling reaction [7,15,16] and as the electrocatalysts in the MOR [8,25a], but to the best of our knowledge, application of these thin films in the degradation of dyes is rare. In this study, application of pure Pt thin film and platinum- based alloys such as PtPd, $PtFeFe_2O_3$, PtNi, PtAu, and also Pd/β-cyclodextrin thin films were investigated in the degradation of MO and the rate constants for catalyzed reactions were determined and compared with MR degradation results. Also, the effect of the degradation of MO on the morphology of metallic nanoalloy catalysts was investigated.

This thin film effectively catalyzed the reduction of MO to N,N-dimethyl-1,4-phenylenediamine and sodium sulfanilate (Scheme 15) in the presence of reducing agent, $NaBH_4$ [13].

TEM and SEM images show the effect of MO degradation on the morphology of the as-prepared thin films (Figs. 24-25 and Table 5).

UV-Vis absorption spectra for the degradation of MO azo dye by $NaBH_4$ (0.1 M) in the presence of Pd/β-cyclodextrin thin film at 25 °C is shown in Fig. 26a. Also, Plot of A *versus* time for the kinetic study of the reaction of MO and $NaBH_4$ (0.001 M) in the presence of this catalyst is shown in Fig. 26b. The apparent rate constant is observable in Table 6. Also, recyclability of these catalysts is shown in Fig. 27 and Table 7.

Progressing dye degradation and nitrophenols reduction reactions by the inclusion complex formation in the presence of Pd/β-cyclodextrin thin film is illustrated in Scheme 16.

In another investigation, a nanoneedle Cu(0)/CuS nanohybrid thin film was synthesized from the reaction of $[Cu(PPh_3)_3I]$ complex with Na_2S at the interface between toluene and water at room temperature. Figure 28 shows the TEM image.

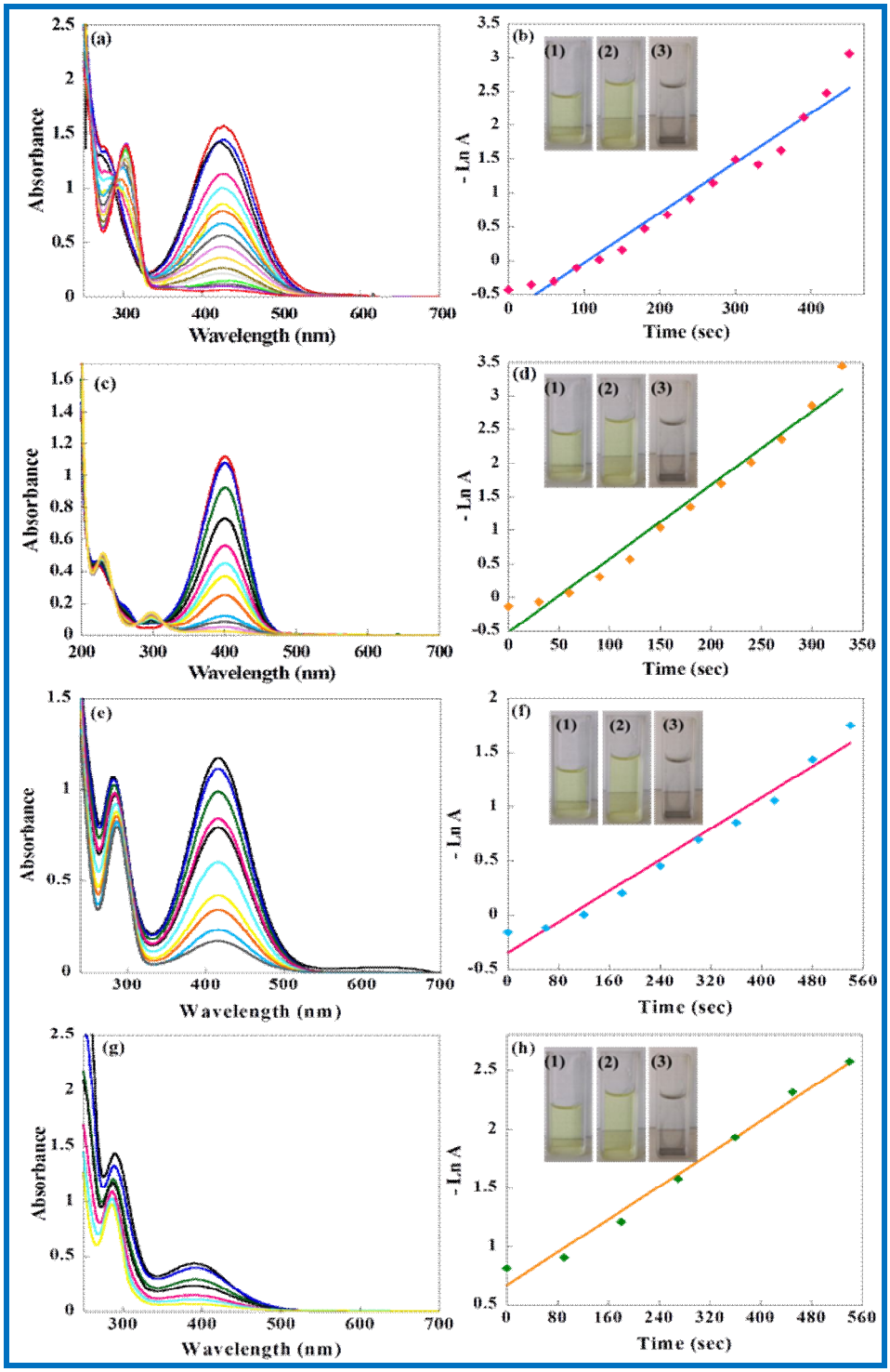

Fig. 22. UV-Vis absorption spectra for the reduction of (a) 4-Cl-2-nitrophenol, (c) 4-NP, (e) *o*-nitrophenol, (g) *m*-nitrophenol (0.2 mM) using aqueous solution of $NaBH_4$ (15 mM) in the presence of Pd/β-cyclodextrin thin film at 25 °C, (b, d, f, h) Plot of -Ln A *versus* time for the related nitroaromatic compounds [28].

Table 4. Comparison of Apparent Rate Constants for 4-NP[a] Reduction with Different Thin Film Nanocatalysts

Entry	Composition	Metal loading (μg)[b]	Apparent rate constant (s^{-1})	Ref.
1	PtPdFe	2.5	3.00×10^{-2}	[18]
2	PdPtZn	2.8	7.5×10^{-3}	[18]
3	PdCuFe/RGO	2.8	8.9×10^{-3}	[18]
4	PtNi	2.1	2.7×10^{-3}	[18]
5	PdZn	2.0	2.96×10^{-3}	[18]
6	PtZn	2.1	4.45×10^{-3}	[18]
7	Pd/RGO	2.5	4.52×10^{-3}	[18]
8	PtCu/RGO	2.6	8.02×10^{-3}	[18]
9	PtCu	2.9	7.3×10^{-3}	[18]
10	PtCo	2.5	1.38×10^{-2}	[18]
11	PdCu	2.5	4.66×10^{-3}	[18]
12	PdCu/RGO	2.2	7.47×10^{-3}	[18]
13	PtCu/AC	2.2	3.39×10^{-3}	[18]
14	Pt/RGO-AC	2.0	1.38×10^{-2}	[18]
15	Pt/RGO	2.2	5.94×10^{-3}	[18]
16	Pd	3.1	1.02×10^{-3}	[18]
17	Pd/AC	3.0	2.58×10^{-2}	[18]
18	PtPdCu	2.5	8.10×10^{-3}	[18]
19	Pd NPs@black tea	2000	5.90×10^{-4}	[108]
20	PdCuO NPs	7000	5.50×10^{-2}	[109]
21	Pt/AC	2.1	3.84×10^{-3}	[5]
22	Pt	3.2	1.98×10^{-3}	[5]
23	Au/RGO	-	0.9×10^{-3}	[110]
24	Pt/RGO	-	2.9×10^{-3}	[110]
25	Pt/C	-	1.0×10^{-3}	[110]
26	Pt Pure	4.0	0.129×10^{-3}	[105]
27	NiPt NPs	4.0	0.159×10^{-3}	[105]
28	PtZnSn	3.8	4.66×10^{-3}	[11]
29	Pd/$[C_2NH_2mim][Br]$	1.4	2.82×10^{-2}	[26]
30	Pd/$[C_8mim][Cl]$	1.0	7.49×10^{-4}	[26]
31	Pd/$[C_8mim][BF_4]$	1.0	2.37×10^{-4}	[26]
32	Pt/$[C_2NH_2mim][Br]$	1.2	4.47×10^{-3}	[27]
33	Pt/$[C_8mim][Cl]$	1.0	5.27×10^{-3}	[27]
34	Pt/$[C_8mim][BF_4]$	1.0	4.44×10^{-3}	[27]
35	Pd/β-cyclodextrin	2.0	1.09×10^{-2}	[28]

[a]You can refer to the related references to find the rate constants for other nitrophenol derivatives in the presence of the above thin films, [b]Obtain from ICP.

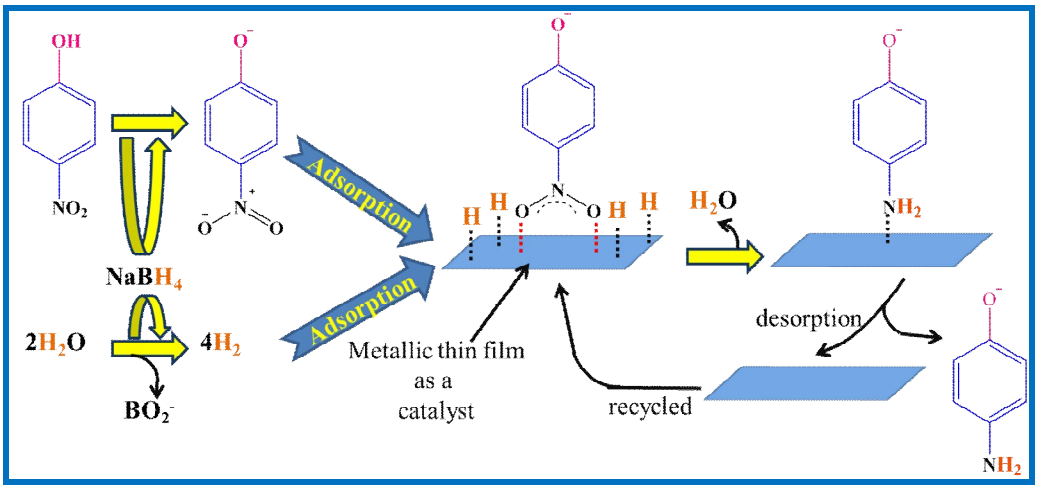

Scheme 13. Mechanism for the reduction of 4-NP on the surface of catalyst

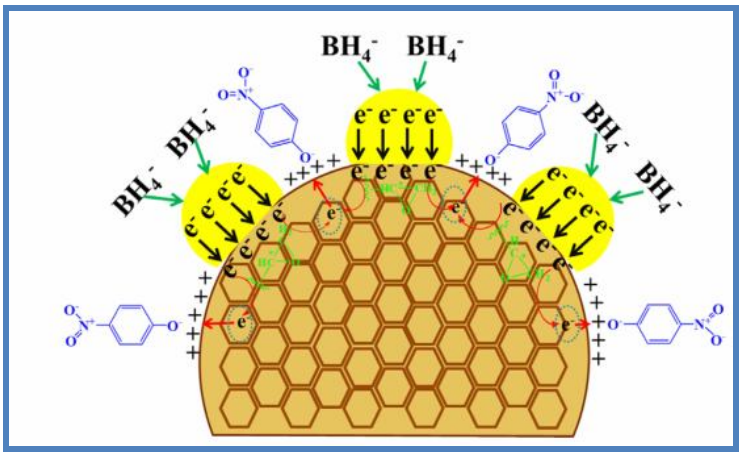

Scheme 14. Details for the mechanism of the reduction of 4-NP on NPs/RGO surfaces [18]

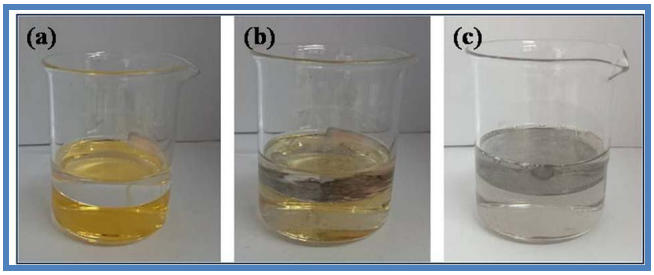

Fig. 23. (a) [$Cl_2Pt(cod)$] complex in toluene (top phase) and MO solution (bottom phase), (b) degradation of MO and formation of Pt thin film simultaneously, 30 s after the beginning of the addition of $NaBH_4$ and (c) complete MO reduction and thin film formation after 2 min [13].

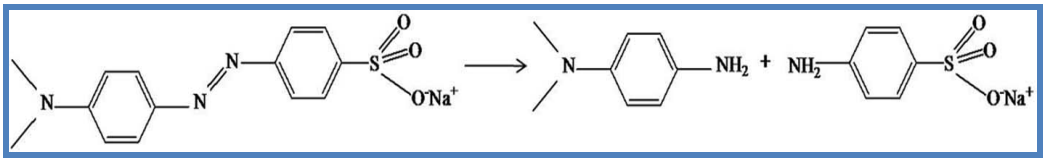

Scheme 15. Reduction of MO to N,N-dimethyl-1,4-phenylenediamine and sodium sulfanilate in the presence of $NaBH_4$ [13].

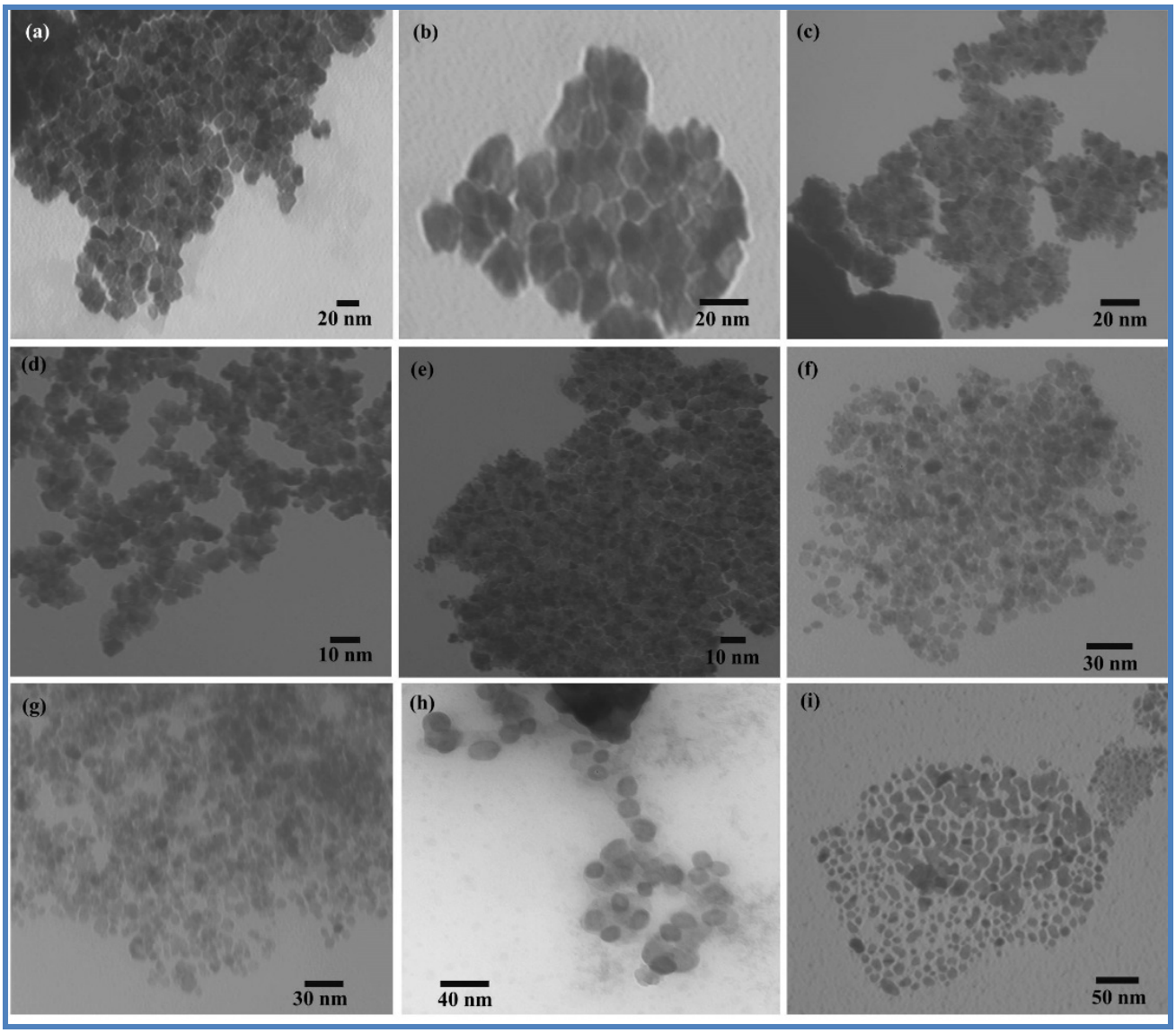

Fig. 24. TEM image of (a,b) hexagonal Pt nanostructured thin film, (c, d, e) PtPd, (f, g) $PtFeFe_2O_3$, (h) PtNi and (i) PtAu thin films in the presence of degraded MO [13].

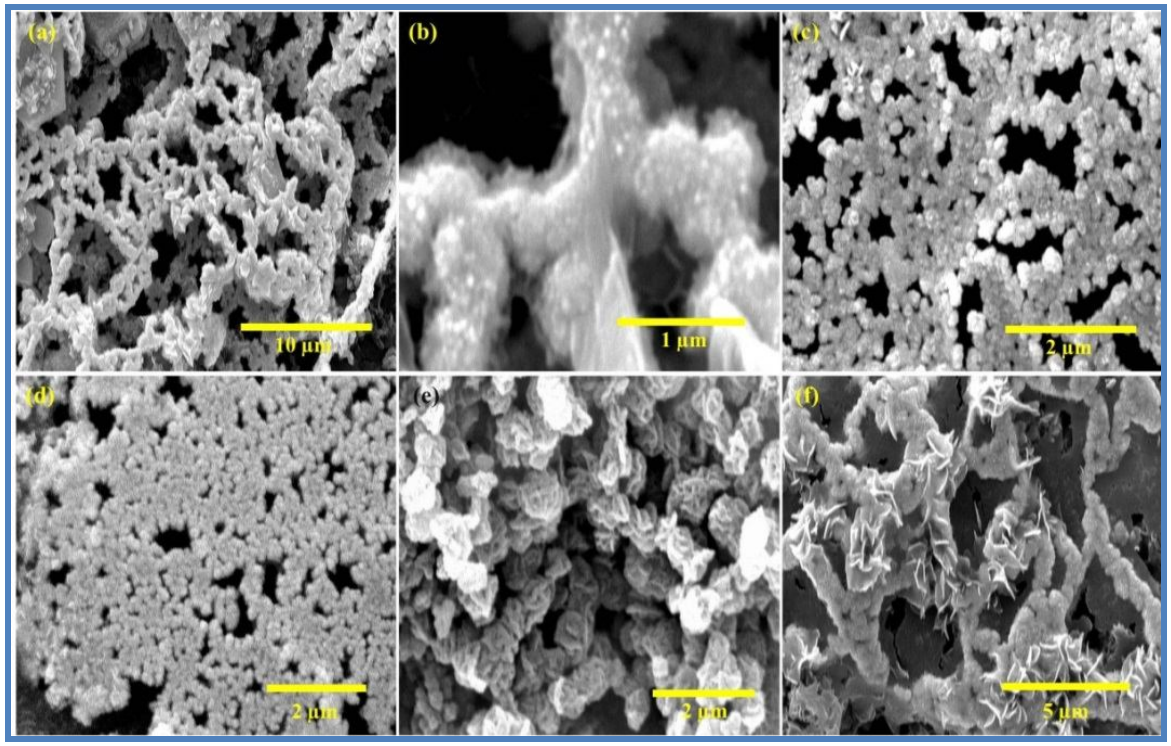

Fig. 25. SEM images of (a,b) Pt, (c) PtPd (d) $PtFeFe_2O_3$, (e) PtNi and (f) PtAu nanostructured thin films in the presence of degraded MO [13].

Table 5. Effect of MO Degradation on the Morphology and Size of the Thin Films [13]

Entry	Thin Film	Morphology	Size (nm)
1	Pt	Spherical NPs	15
2	PtPd	Snowman like-shaped nanostructures	40
3	PtNi	Spherical NPs	25
4	$PtFeFe_2O_3$	Spherical NPs	20
5	Pt/MO	Hexagonal	11
6	PtPd/MO	Polygonal structure	3
7	PtNi/MO	Spherical NPs	17
8	$PtFeFe_2O_3$/MO	Spherical NPs	4
9	PtAu/MO	Spherical NPs	5

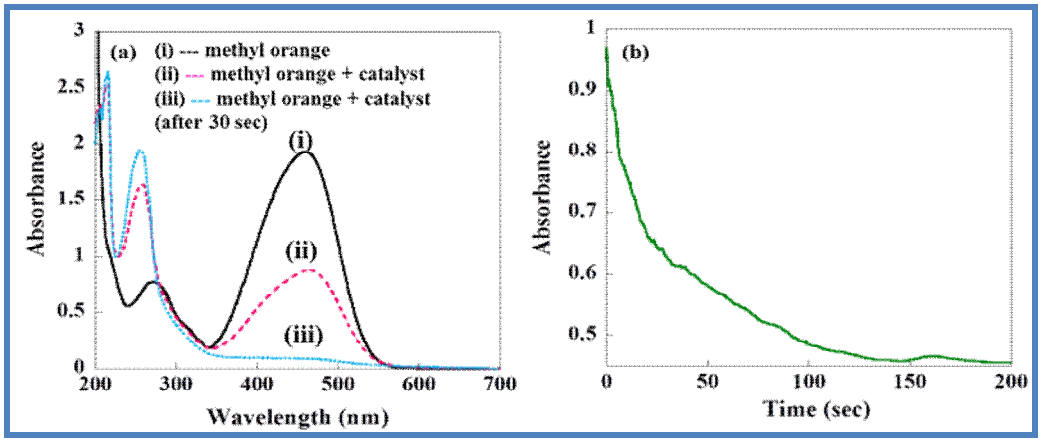

Fig. 26. UV-Vis absorption spectra for the MO degradation by $NaBH_4$ in the presence of Pt/β-cyclodextrin thin film at r.t. (time interval = 30s), (b) Plot of A *versus* time for the kinetic study of the reaction of MO degradation ''A'' stands for absorbance at λ = 464 nm for different times [28].

Table 6. Comparison of Apparent Rate Constants for MO and MR Degradation at Nanostructured Thin Films Obtained from Liquid-liquid Interface [13]

Entry	Catalyst	k_{obs} $(s^{-1})^a$	k_{obs} $(s^{-1})^d$	Ref.[a]
1	Pt thin film	$1.09 \times 10^{-2} \pm 0.0001$	$4.86 \times 10^{-3} \pm 0.00006$	[13]
2	PtPd thin film	$2.02 \times 10^{-1} \pm 0.02$	$4.75 \times 10^{-2} \pm 0.0001$	[13]
3	$PtFeFe_2O_3$ thin film	$1.80 \times 10^{-2} \pm 0.0003$	$9.70 \times 10^{-3} \pm 0.00002$	[13]
4	PtNi thin film	$3.75 \times 10^{-2} \pm 0.0002$	$7.45 \times 10^{-3} \pm 0.00004$	[13]
5	PtAu thin film	$1.70 \times 10^{-2} \pm 0.002$	$4.34 \times 10^{-2} \pm 0.0001$	[13]
6	MZVI[b]	8.30×10^{-4}	-	[111]
7	NZVI[c]	5.60×10^{-3}	-	[111]
8	Ag NPs	8.50×10^{-3}	-	[112]
9	Pd/β-cyclodextrin thin film	1.85×10^{-2}	-	[28]

In the presence of (a) MO dye; (b) MZVI: microscale zero-valent iron, (c) NZVI: nanoscale zero-valent iron; (d) MR dye.

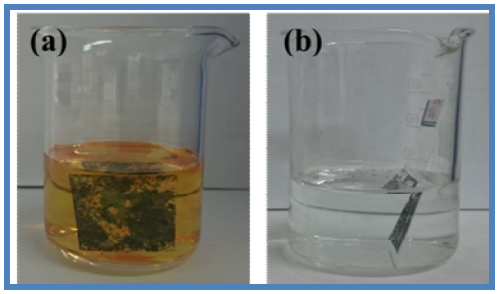

Fig. 27. Catalysts reusability for MO degradation [13].

Table 7. Reusability of Thin Films in the Presence of MO and MR [13]

Entry	Catalyst	Number of cycles	
1	Pt thin film	2[a]	2[b]
2	PtPd thin film	3[a]	3[b]
3	$PtFeFe_2O_3$ thin film	6[a]	8[b]
4	PtNi thin film	4[a]	2[b]
5	PtAu thin film	4[a]	5[b]

In the presence of (a) MO and (b) MR dye.

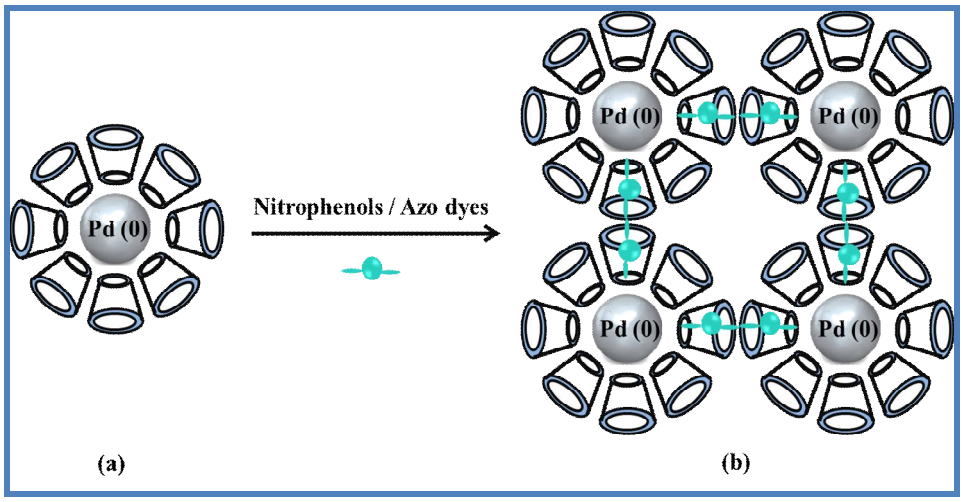

Scheme 16. Inclusion complex formation using Pd/β-cyclodextrin thin film as a catalyst in the presence of nitrophenols or azo dyes as guest molecules [28]

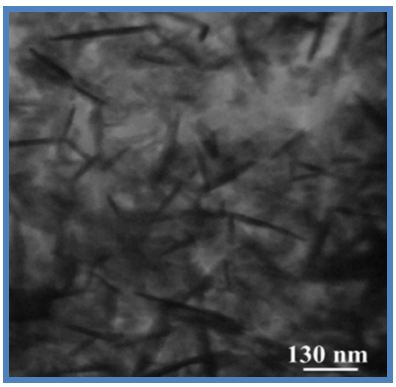

Fig. 28. TEM characterization of Cu(0)/CuS nanohybrid thin film [20].

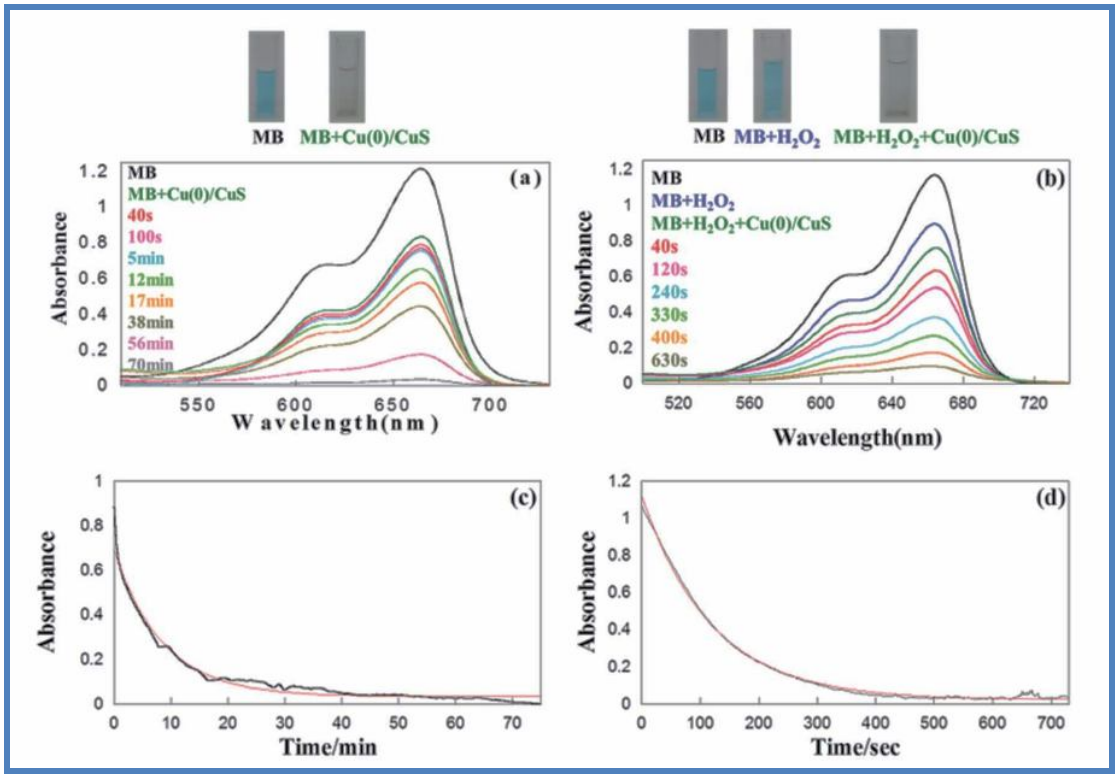

Fig. 29. Degradation of methylene blue (MB) dye (a) plot of absorbance (A) *vs*. wavelength and the inset image indicates the decolorisation reaction in the absence of H_2O_2, (b) plot of absorbance (A) *vs*. wavelength and the inset image indicates the decolorisation reaction in the presence of H_2O_2, (c) plot of absorbance (A) *vs*. time (t) in the absence of H_2O_2 and (d) plot of absorbance (A) *vs*. time (t) in the presence of H_2O_2 [20].

Table 8. Dye Degradation in the Presence of Cu(0)/CuS Nanoneedles at 25 °C [20]

Dye	Peroxide	k_{app} (s^{-1})
MB[a]	-	1.97×10^{-3}
MB[a]	H_2O_2	8.40×10^{-3}
MG[b]	-	6.67×10^{-4}
MG[b]	H_2O_2	6.82×10^{-3}
BG[c]	H_2O_2	5.48×10^{-3}
MR[d]	H_2O_2	1.36×10^{-2}

[a]MB: methylene blue; [b]MG: malachite green; [c]BG: brilliant green; [d]MR: methyl red.

The catalytic activity of Cu(0)/CuS nanoneedles was investigated in the degradation of dyes in the presence or absence of H_2O_2. On the basis of comparative kinetic studies, the following trend was obtained for the degradation of different dyes in the presence of H_2O_2 and CuS catalyst (Fig. 29 and Table 8): neutral dyes > cationic dyes > anionic dyes [20].

In our recent investigation, PtSn thin films were formed from the reaction of SnX_2 (X = Cl, Br) with [$PtMe_2$(bipy)], (bipy = 2,2'-bipyridine), in the presence or absence of GO support with effective catalytic activity in MOR [113].

SUMMARY

In this general report, organometallic precursors were used for the formation of a wide range of nanostructures and applied in various catalytic reactions. Catalytic activity of noble and non-precious transition metallic alloy thin films has been studied for converting the nitrophenol compounds to aminophenols in the presence of $NaBH_4$. Also, these thin films showed interesting electrocatalytic activity in MOR. The catalysts formed from liquid-liquid interface strategy are promising electrocatalysts for fuel cells and sensors. Furthermore, some of the as-synthesized nanostructures can be applied as catalyst in C-C cross coupling reactions such as Suzuki-Miyaura and Sonogashira couplings. Some severe problems for pharmaceutical industries that limit their applications are: the high cost Pd cannot be recycled and reused, difficult extraction from reaction mixture which causes by homogeneous Pd catalysts during C-C coupling reactions. In contrast with homogeneous systems, catalyst stability, easy extraction from the reaction mixture even by simple filtration and catalysts reproducibility for several reactions are the advantages of heterogeneous catalysts. In this investigation, we reported the use of some catalysts in a safe solvent and eco-friendly medium. These recyclable heterogeneous catalysts showed efficient catalytic activity for the Sonogashira carbon-carbon coupling reaction of a wide range of aryl halides with phenylacetylene. It can be expected that these kinds of catalysts will reach wide applications in the near future. In brief, the summary of our key findings are these important facts: (i) Stabilization of metallic NPs and alloys on support surfaces such as graphene oxide, aminoclay, ionic liquids or cyclodextrins can increase the catalytic activity by increasing the stability, dispersion and preventing from aggregation. (ii) Alloying effects and morphology shows that alloyed nanostructures can be efficient like noble metal catalysts in catalytic applications. (iii) Applying liquid-liquid interface strategy to synthesize the catalysts shows that notably thin films fabricated by this method show higher quality in comparison with the thin films fabricated by other methods. This study highlights the value and importance of nano alloy thin films and their key ability in the progress of various catalytic reactions. We hope that they can be applied for other important catalytic applications.

ABBREVIATIONS

nanoparticles	NPs
direct methanol fuel cell	DMFC
cis,cis-1,5-cyclooctadiene	cod
triphenylphosphine	PPh_3
acetylacetonate	acac
X-ray diffraction	XRD
transmission electron microscopy	TEM
nanobranch	NB
alloy nanosheets	ANSs
graphene oxide	GO
aminoclay	AC
ionic liquids	ILs
reduced-graphene oxide- aminoclay	RGO-AC
reduced-graphene oxide	RGO
field emission- scanning electron microscopy	FE-SEM
selected area electron diffraction	SAED
polyvinylpyrrolidone	PVP
1-aminoethyl-3-methyl-imidazolium bromide	[C_2NH_2mim][Br]
1-methyl-3-octylimidazolium chloride	[C_8mim][Cl]
1-methyl-3-octylimidazolium tetrafluoroborate	[C_8mim][BF_4]
zeolitic imidazolate framework-8	ZIF-8
3-(aminomethyl)pyridine	3-ampy
2-phenylpyridine	C^N
dimethylsulfoxide	dmso
amine functionalized GO	*f*-GO

(3-aminopropyl)triethoxysilane	APTES
X-ray photoelectron spectroscopy	XPS
energy dispersive analysis of X-ray	EDAX
direct alcohol fuel cells	DAFCs
methanol oxidation reaction	MOR
forward anodic peak current	J_f
backward peak current	J_b
ethanol	EtOH
Santa Barbara amorphous type silica	SBA-15
tetra(ethylene glycol)	TEG
generation-3	G-3
sodium acetate	NaOAc
dimethylformamide	DMF
methanol	MeOH
N-heterocyclic carbene	NHC
cetyltrimethylammonium bromide	CTAB
dimethyl acetamide	DMA
montmorillonite	MMT
4-nitrophenol	4-NP
4-aminophenol	4-AP
methyl orange	MO
methyl red	MR
microscale zero-valent iron	MZVI
nanoscale zero-valent iron	NZVI
methylene blue	MB
malachite green	MG
brilliant green	BG
2,2'-bipyridine	bipy

ACKNOWLEDGEMENTS

We would like to thank Shiraz University Research Council, Iran National Science Foundation (INSF) (Grant No. 97006154), Iran Science Elites Federation and the Iranian Nanotechnology Initiative Council for their support.

REFERENCES

[1] B. Cormary, F. Dumestre, N. Liakakos, K. Soulantica, B. Chaudret, Dalton Trans. 42 (2013) 12546.

[2] T. Zhai, L. Li, Y. Ma, M. Liao, X. Wang, X. Fang, J. Yao, Y. Bando, D. Golberg, Chem. Soc. Rev. 40 (2011) 2986.

[3] C.N.R. Rao, A. Govindaraj, Adv. Mater. 21 (2009) 4208.

[4] S. Hu, H. Liu, P. Wang, X. Wang, J. Am. Chem. Soc. 135 (2013) 11115.

[5] S.J. Hoseini, M. Rashidi, M. Bahrami, J. Mater. Chem. 21 (2011) 16170.

[6] S.J. Hoseini, N. Mousavi, M. Roushani, L. Mosaddeghi, M. Bahrami, M. Rashidi, Dalton Trans. 42 (2013) 12364.

[7] S.J. Hoseini, M. Dehghani, H. Nasrabadi, Catal. Sci. Technol. 4 (2014) 1078.

[8] S.J. Hoseini, M. Bahrami, M. Zanganeh, M. Roushani, M. Rashidi, RSC Adv. 6 (2016) 45753.

[9] S.J. Hoseini, M. Bahrami, M. Maddahfar, R. Hashemi Fath, M. Roushani, Appl. Organomet. Chem. 32 (2018) e3894.

[10] S.J. Hoseini, Z. Barzegar, M. Bahrami, M. Roushani, M. Rashidi, J. Organomet. Chem. 769 (2014) 1.

[11] S. Saberi Sarmoor, S.J. Hoseini, R. Hashemi Fath, M. Roushani, M. Bahrami, Appl. Organomet. Chem. 32 (2018) e3979.

[12] S.J. Hoseini, M. Bahrami, M. Roushani, RSC Adv. 4 (2014) 46992.

[13] M. Bahrami, S.J. Hoseini, Appl. Organomet. Chem. 32 (2018) e3920.

[14] S.J. Hoseini, N. Aramesh; M. Bahrami, Appl. Organomet. Chem. 31 (2017) e3675.

[15] P. Fatahi, S.J. Hoseini, Appl. Organomet. Chem. 32 (2018) e4187.

[16] S.J. Hoseini, E. Jahanshahi, R. Hashemi Fath, Appl. Organomet. Chem. 31 (2017) e3718.

[17] S.J. Hoseini, B. Habib Agahi, Z. Samadi Fard, R. Hashemi Fath, M. Bahrami, Appl. Organomet. Chem. 31 (2017) e3607.

[18] S.J. Hoseini, M. Bahrami, N. Sadri, N. Aramesh, Z. Samadi Fard, H. Rafatbakhsh Iran, B. Habib Agahi, M. Maddahfar, M. Dehghani, A. Zarei Baba Arabi, N. Heidari, S.F. Hashemi Fard, Z. Moradi, J. Colloid Interface Sci. 513 (2018) 602.

[19] S.J. Hoseini, A. Zarei, H. Rafatbakhsh Iran, Appl. Organomet. Chem. 29 (2015) 489.

[20] S.J. Hoseini, R. Hashemi Fath, RSC Adv. 6 (2016) 76964.

[21] C.N.R. Rao, K.P. Kalyanikutty, Acc. Chem. Res. 41 (2008) 489.

[22] C.N.R. Rao, G.U. Kulkarni, V.V. Agrawal, U.K. Gautam, M. Ghosh, U. Tumkurkar, J. Colloid Interface Sci. 15 (2005) 305.

[23] C.N.R. Rao, V.V. Agrawal, K. Biswas, U.K. Gautam, M. Ghosh, A. Govindaraj, G.U. Kulkarni, K.P. Kalyanikutty, K. Sardar, S.R.C. Vivekchand, Pure Appl. Chem. 78 (2006) 1619.

[24] U.K. Gautam, M. Ghosh, C.N.R. Rao, Chem. Phys. Lett. 381 (2003) 1.

[25] a) S.J. Hoseini, M. Bahrami, M. Dehghani, RSC Adv. 4 (2014) 13796; b) S.J. Hoseini, M. Bahrami, Z. Samadi Fard, S.F. Hashemi Fard, M. Roushani, B. Habib Agahi, R. Hashemi Fath, S. Saberi Sarmoor, Int. J. Hydrogen Energy 43 (2018) 15095.

[26] M. Gheitasi Zarooni, S.J. Hoseini, M. Bahrami, M. Roushani, S.M. Nabavizadeh, J. Inorg. Organomet. Polym. (2020) https://doi.org/10.1007/s10904-020-01514-9.

[27] S. Hamzepour Sharfand, S.J. Hoseini, M. Bahrami, Polyhedron 151 (2018) 483.

[28] A. Zare Asadabadi, S.J. Hoseini, M. Bahrami, S.M. Nabavizadeh, New J. Chem. 43 (2019) 6513.

[29] S.J. Hoseini, M. Bahrami, S.M. Nabavizadeh, New J. Chem. 43 (2019) 15811.

[30] a) M. Faraday, Philos. Trans. R. Soc. London 147 (1857) 145; b) V. Divya, M.V. Sangaranarayanan, J. Nanosci. Nanotechnol. 15 (2015) 6863.

[31] L.L. Zhang, Y.H. Jiang, Y.L. Ding, M. Povey, D. York, J. Nanopart. Res. 479 (2007) 9.

[32] H.S. Zhou, I. Honma, H. Komiyama, J.W. Haus, J. Phys. Chem. 97 (1993) 895.

[33] C.N.R. Rao, P.J. Thomas, G.U. Kulkarni, Nanocrystals: Synthesis, Properties and Applications, Springer-Verlag Berlin Heidelberg 2007, P. 29.

[34] H.I. Schlesinger, H.C. Brown, A.E. Finholt, J. Am. Chem. Soc. 75 (1953) 215.

[35] J. Turkevich, P.C. Stevenson, J. Hillier, J. Discuss. Farad. Soc. 11 (1951) 55.

[36] K. Piradashvili, E.M. Alexandrino, F.R. Wurm, K. Landfester, Chem. Rev. 116 (2016) 2141.

[37] A. Berduque, A. Sherburn, M. Ghita, R.A.W. Dryfe, D.W.M. Arrigan, Anal. Chem. 77 (2005) 7310.

[38] M.A. Lopez-Quintela, C. Tojo, M.C. Blanco, L.G. Rio, J.R. Leis, Curr. Opin. Colloid Interface Sci. 9 (2004) 264.

[39] E. Scoppola, E.B. Watkins, R.A. Campbell, O. Konovalov, L. Girard, J.F. Dufreche, G. Ferru, G. Fragneto, O. Diat, Angew. Chem. 128 (2016) 9472.

[40] L. Leclercq, A. Mouret, A. Proust, V. Schmitt, P. Bauduin, J.M. Aubry, V. Nardello-Rataj, Chem. Eur. J. 18 (2012) 14352.

[41] C.N.R. Rao, G.U. Kulkarni, P.J. Thomas, V.V. Agarwal, U.K. Gautam, M. Ghosh, Curr. Sci. 85 (2003) 1041.

[42] V.V. Agrawal, P. Mahalakshmi, G.U. Kulkarni, C.N.R. Rao, Langmuir 22 (2006) 1846.

[43] U.K. Gautam, M. Ghosh, C.N.R. Rao, Langmuir 20 (2004) 10775.

[44] V.V. Agrawal, G.U. Kulkarni, C.N.R. Rao, J. Phys. Chem. B 109 (2005) 7300.

[45] K.P. Kalyanikutty, U.K. Gautam, C.N.R. Rao, Solid State Sci. 8 (2006) 296.

[46] C.N.R. Rao, H.S.S.R. Matte, R. Voggu, A. Govindaraj, Dalton Trans. 41 (2012) 5089.

[47] A.G. Volkov, Liquid Interfaces in Chemical, Biological and Pharmaceutical Applications, edited by M. Dekker, New York, USA, 2001.

[48] F. Bresme, M. Oettel, J. Phys. Condens. Matter 19 (2007) 1.

[49] Y. Grunder, M.D. Fabian, S.G. Booth, D. Plana, D.J. Fermin, P.I. Hill, R.A.W. Dryfe, Electrochim. Acta 110 (2013) 809.

[50] J.J. Nieminen, I. Hatay, P.Y. Ge, M.A. Mendez, L. Murtomaki, H.H. Girault, Chem. Commun. 47 (2011) 5548.

[51] K. Isobe, P.M. Bailey, P.M. Maitlis, J. Chem. Soc., Chem. Commun. (1981) 808.

[52] G. Schmid, R. Pfeil, R. Boese, F. Brandermann, S. Meyer, G.H.M. Calis, J.W.A. Van der Velden, Chem. Ber. 114 (1981) 3634.

[53] B. Chaudret, D.J. Cole-Hamilton, G. Wilkinson, J. Chem. Soc., Dalton Trans. (1978) 1739.

[54] H.S. Booth, L.F. Audrieth, J.C. Bailar, Inorganic synthesis, McGraw-Hill, New York and London 1939.

[55] A.P. Ginsberg, Inorganic Syntheses. New Jersey: Inorganic Syntheses, Inc. 1990.

[56] M.K. Chaudhuri, S.K. Ghosh, J. Chem. Soc. Dalton Trans. (1983) 839.

[57] Y. Xiong, H. Cai, B.J. Wiley, J. Wang, M.J. Kim, Y. Xia, J. Am. Chem. Soc. 129 (2007) 3665.
[58] M. Grzelczak, J. Perez-Juste, P. Mulvaney, L.M. Liz-Marzan, Chem. Soc. Rev. 37 (2008) 1783.
[59] S.K. Meena, S. Celiksoy, P. Schafer, A. Henkel, C. Sonnichsen, M. Sulpizi, Phys. Chem. Chem. Phys. 18 (2016) 13246.
[60] C. Wang, D. van der Vliet, K.L. More, N.J. Zaluzec, S. Peng, S. Sun, H. Daimon, G. Wang, J. Greeley, J. Pearson, A.P. Paulikas, G. Karapetrov, D. Strmcnik, N.M. Markovic, V.R. Stamenkovic, Nano Lett. 11 (2011) 919.
[61] X.L. Cai, C.H. Liu, J. Liu, Y. Lu, Y.N. Zhong, K.Q. Nie, J.L. Xu, X. Gao, X.H. Sun, S.D. Wang, Nano-Micro Lett. 9 (2017) 48.
[62] A.K. Singh, Q. Xu, Chem. Cat. Chem. 5 (2013) 652.
[63] H. Zhang, M. Jin, H. Liu, J. Wang, M.J. Kim, D. Yang, Z. Xie, J. Liu, Y. Xia, ACS Nano 5 (2011) 8212.
[64] D. Huang, X. Bai, L. Zheng, J. Phys. Chem. C 115 (2011) 14641.
[65] J.N. Zheng, L.L. He, F.Y. Chen, A.J. Wang, M.W. Xue, J.J. Feng, J. Mater. Chem. A 2 (2014) 12899.
[66] X. Lu, X. Bian, G. Nie, C. Zhang, C. Wang, Y. Wei, J. Mater. Chem. 22 (2012) 12723.
[67] K.K.R. Datta, A. Achari, M. Eswaramoorthy, J. Mater. Chem. A 1 (2013) 6707.
[68] G. Law, P.R. Watson, Langmuir 17 (2001) 6138.
[69] S.J. Hoseini, H. Ghanavat Khozestan, R. Hashemi Fath, RSC Adv. 5 (2015) 47701.
[70] S.J. Hoseini, V. Heidari, H. Nasrabadi, J. Mol. Catal. A Chem. 396 (2015) 90.
[71] R. Hashemi Fath, S.J. Hoseini, J. Organomet. Chem. 828 (2017) 16.
[72] R. Hashemi Fath, S.J. Hoseini, Appl. Organomet. Chem. 32 (2018) e3964.
[73] S.S. Siwal, S. Thakur, Q.B. Zhang, V.K. Thakur, Mater. Today Chem. 14 (2019) 100182.
[74] N.A. Karim, S.K. Kamarudin, Appl. Energy 103 (2013) 212.
[75] Z.A.C. Ramli, S.K. Kamarudin, Nanoscale Res. Lett. 13 (2018) 410.
[76] X. Ren, Q. Lv, L. Liu, B. Liu, Y. Wang, A. Liu, G. Wu, Sustain. Energ. Fuels 4 (2020) 15.
[77] D.H. Kwak, Y.W. Lee, K.H. Lee, A.R. Park, J.S. Moon, K.W. Park, Int. J. Electrochem. Sci. 8 (2013) 5102.
[78] H. Li, D. Kang, H. Wang, R. Wang, Int. J. Electrochem. Sci. 6 (2011) 1058.
[79] O. Lupan, L. Chow, G. Chai, H. Heinrich, Chem. Phys. Lett. 465 (2008) 249.
[80] T. Maiyalagan, T.O. Alaje, K. Scott, J. Phys. Chem. C 116 (2012) 2630.
[81] H. Sun, J. You, M. Yang, F. Qu, J. Power Sources 205 (2012) 231.
[82] X. Ge, R. Wang, P. Liu, Y. Ding, Chem. Mater. 19 (2007) 5827.
[83] Y. Kang, J.B. Pyo, X. Ye, T.R. Gordon, C.B. Murray, ACS Nano 6 (2012) 5642.
[84] A.J. Bard, L.R. Faulkner, Electrochemical Methods Fundamentals and Application, 1980, p. 236.
[85] N. Ghanbari, S.J. Hoseini, M. Bahrami, Ultrason. Sonochem. 39 (2017) 467.
[86] R.K. Rai, K. Gupta, S. Behrens, J. Li, Q. Xu, S.K. Singh, ChemCatChem. 7 (2015) 1806.
[87] A. Fihri, M. Bouhrara, B. Nekoueishahraki, J.M. Basset, V. Polshetttiwar, Chem. Soc. Rev. 40 (2011) 5181.
[88] J. Xiang, P. Li, H. Chong, L. Feng, F. Fu, Z. Wang, S. Zhang, M. Zhu, Nano Res. 7 (2014) 1337.
[89] M. Nasrollahzadeh, S.M. Sajadi, A. Rostami-Vartooni, M. Khalaj, J. Mol. Catal. A: Chem. 396 (2015) 31.
[90] J. Zhou, X. Guo, C. Tu, X. Li, H. Sun, J. Organomet. Chem. 694 (2009) 697.
[91] V. Gaikwad, R. Kurane, J. Jadhav, R. Salunkhe, G. Rashinkar, Appl. Catal. A 451 (2013) 243.
[92] A.M. Thomas, A. Sujatha, G. Anilkumar, RSC Adv. 4 (2014) 21688.
[93] R. Ciriminna, V. Pandarus, G. Gingras, F. Beland, P.D. Cara, M. Pagliaro, Chem. Eng. 1 (2013) 57.
[94] A. Elhage, A.E. Lanterna, J.C. Scaiano, ACS Sustainable Chem. Eng. 6 (2018) 1717.
[95] D. Wang, S. Gao, Org. Chem. Front. 1 (2014) 556.
[96] A.A. Liori, I.K. Stamatopoulos, A.T. Papastavrou, A. Pinaka, G.C. Vougioukalakis, Eur. J. Org. Chem. 2018 (2018) 6134.
[97] M.B. Thathagar, J. Beckers, G. Rothenberg, Green

Chem. 6 (2004) 215.
[98] Y. Liang, Y.X. Xie, J.H. Li, J. Org. Chem. 71 (2006) 379.
[99] D.I. Sharapa, D.E. Doronkin, F. Studt, J.D. Grunwaldt, S. Behrens, Adv. Mater. 31 (2019) 1807381.
[100] R. Hashemi Fath, S.J. Hoseini, New J. Chem. 41 (2017) 3392.
[101] R.G. Heidenreich, K. Kohler, J.G.E. Krauter, J. Pietsch, Synlett. 7 (2002) 1118.
[102] M. Gholinejad, J. Ahmadi, Chem. Plus Chem. 80 (2015) 973.
[103] W. Xu, H. Sun, B. Yu, G. Zhang, W. Zhang, Z. Gao, ACS Appl. Mater. Interfaces 6 (2014) 20261.
[104] C. Zhou, H. Wang, F. Peng, J. Liang, H. Yu, J. Yang, Langmuir 25 (2009) 7711.
[105] S.K. Ghosh, M. Mandal, S. Kundu, S. Nath, T. Pal, Appl. Catal. A Gen. 268 (2004) 61.
[106] S. Dutta, S. Sarkar, C. Ray, A. Roy, R. Sahoo, T. Pal, ACS Appl. Mater. Interfaces 6 (2014) 9134.
[107] N. Pradhan, A. Pal, T. Pal, Langmuir 17 (2001) 1800.
[108] S. Lebaschi, M. Hekmati, H. Veisi, J. Colloid Interface Sci. 485 (2017) 223.
[109] M. Nasrollahzadeh, S.M. Sajadi, A. Rostami-Vartooni, M. Bagherzadeh, J. Colloid Interface Sci. 448 (2015) 106.
[110] Q. Liu, Y.R. Xu, A.J. Wang, J.J. Feng, RSC Adv. 5 (2015) 96028.
[111] Y.H. Shih, C.P. Tso, L.Y. Tung, J. Environ. Eng. Manage. 20 (2010) 137.
[112] A. Bhankhar, M. Giri, K. Yadav, N. Jaggi, Indian J. Phys. 88 (2014) 1191.
[113] N. Aramesh, S.J. Hoseini, H.R. Shahsavari, S.M. Nabavizadeh, M. Bahrami, M.R. Halvagar, E. De Giglio, M. Latronico, P. Mastrorilli, Inorg. Chem. 59 (2020) 10688.